AIAA SciTech Forum
9 - 13 January 2017, Grapevine, Texas
55th AIAA Aerospace Sciences Meeting

Modeling of Noise Reduction in Complex Multistream Jets

Dimitri Papamoschou*
University of California, Irvine, Irvine, CA, 92697, USA

The paper presents a low-order prediction scheme for the noise change in multistream jets when the nozzle geometry is altered from a known baseline. The essence of the model is to predict the changes in acoustics due to the redistribution of the mean flow as computed by a Reynolds-Averaged Navier Stokes (RANS) solver. A RANS-based acoustic analogy framework is developed that addresses the noise in the polar direction of peak emission and uses the Reynolds stress as a time-averaged representation of the action of the coherent turbulent structures. The framework preserves the simplicity of the Lighthill acoustic analogy, using the free-space Green's function, while accounting for azimuthal effects via special forms for the space-time correlation combined with source-observer relations based on the Reynolds stress distribution in the jet plume. Results are presented for three-stream jets with offset tertiary flow that reduces noise in specific azimuthal directions. The model reproduces well the experimental noise reduction trends.

Nomenclature

a	=	speed of sound
A	=	cross sectional area; amplitude
C	=	correlation coefficient
D	=	diameter
f	=	cyclic frequency
g	=	principal component of the Reynolds stress
G	=	magnitude of mean velocity gradient
k	=	turbulent kinetic energy
L	=	correlation length scale
M	=	Mach number
M_c	=	convective Mach number
r	=	distance between source and observer
R	=	observer distance in spherical coordinate system; correlation function
p	=	pressure
q'	=	fluctuating velocity component along mean flow gradient
T	=	Lighthill stress tensor
u, v, w	=	velocity components in Cartesian coordinate system
$\mathbf{u}$	=	velocity vector
U	=	fully-expanded velocity
U_c	=	convective velocity
W	=	annulus width
X, Y, Z	=	Cartesian coordinate system
$\mathbf{x}$	=	field point location
y	=	radial coordinate
$\mathbf{y}, \mathbf{y}'$	=	source locations
α	=	acoustic wavenumber $= \omega/a_\infty$
β	=	correlation shape parameter
ϵ	=	dissipation

*Professor, Department of Mechanical and Aerospace Engineering, Fellow AIAA

θ	=	polar angle relative to downstream jet axis
ϑ	=	direction cosine
ϕ	=	geometric azimuthal angle relative to downward vertical
ϕ_g	=	gradient-based azimuthal angle
ρ	=	density
ω	=	angular frequency
Ω	=	specific dissipation = ϵ/k

Subscripts

i, j, k, l	=	correlation indices
0	=	observer
p	=	primary stream
s	=	secondary stream
t	=	tertiary stream
∞	=	ambient

I. Introduction

The exhaust of jet engines continues to be a significant contributor to aircraft noise. The problem is particularly acute for medium-bypass ratio, high-performance turbofan engines that are envisioned to power the next generation of supersonic transports. Even for large-bypass ratio engines on commercial subsonic aircraft, jet noise remains a problem and an active area of research.

For a fixed engine cycle, jet noise reduction is achieved through some type of modification of the exhaust nozzle. Such modifications have included chevrons,[1] fluidic injection,[2] and offset-stream nozzles.[3–9] These approaches have been the topic of numerous experimental and computational investigations. Computational tools like large eddy simulation (LES) have progressed to the point where they can provide high-fidelity time-resolved solutions to the flow field. Coupled with surface-based integration methods, these computations yield far-field noise spectra that are becoming increasingly reliable. However, the computational cost and long turnaround times of LES-based approaches render them impractical for design purposes. There is need for low-order tools that can provide "real time" answers with sufficient accuracy for propulsion design.

The predominant low-order modeling tool used today consists of an acoustic analogy coupled with a Reynolds-Averaged Navier Stokes (RANS) solution of the flow field. Naturally, this approach is built upon layers of assumptions and involves a level of empiricism. The original acoustic analogy formulation by Lighthill[10] uses the free-space Green's function and can yield satisfactory results for round jets.[11] Improvements have included the effect of refraction by the mean flow, which requires solving the linearized Euler equations.[12,13] Simplification is often sought through the locally parallel flow approximation, in which case the Green's function can be reduced to analytical forms. This approach has yielded accurate predictions for jets from round nozzles as well as nozzles with chevrons and fluidic injection.[14] For the chevron and fluidic-injection jets, azimuthal effects on propagation were not considered, which is a reasonable simplification given that the mean flow is mostly axisymmetric.

For asymmetric jets, inclusion of refraction effects becomes a much larger challenge. Yet, it is critical to account for them in some fashion in order to capture the azimuthal variation of noise emission and the noise suppression enabled by offset-stream concepts. Even under the simplification of the parallel-flow approximation, the construction of the Green's functions involves complex numerical procedures.[15] The parallel-flow approximation itself poses the risk of disregarding flow features that could play a critical role in the generation or suppression of noise. Application to three-stream jets with offset tertiary duct has shown initial promise,[7] although the modeled azimuthal directivity was weaker than the experimental one. There is no question that the rigorous acoustic analogy approach that involves numerical solutions for the Green's functions is a direction that should be pursued and ultimately will yield accurate results. However, the computational complexity and cost motivate the search for a simpler option that will give the designer initial guidance in real time, once the RANS solution is available.

The present effort therefore seeks the development of practical tool to predict the changes in acoustics imparted by nozzle modifications, with emphasis on techniques that induce asymmetry in the nozzle plume.

The focus is on predicting the change in *peak noise*, relative to a known reference jet, due to the redistribution of the time-averaged flow field as computed by a Reynolds-Averaged Navier Stokes (RANS) solver. It is widely agreed that the peak noise is generated by coherent turbulent structures, so this will be a central element in the theoretical development. The approach is influenced by the large body of work on acoustic analogy, starting with Lighthill[10] and including Morris and Farrasat,[11] Harper-Bourne[16] and many others cited in following sections. The model maintains the simplicity of the free-space Green's function used in the original Lighthill acoustic analogy and induces azimuthal directivity through a novel formulation of the space-time correlation of the Lighthill stress tensor. Moreover, we avoid the complication of connecting the volumetric source to a surface source in an attempt to induce azimuthal directivity, as was done in a predecessor effort.[17] The present model is based solely on a volumetric source.

II. Framework of the Approach

This section provides context for the analysis that follows. The concepts presented here will have direct impacts on the development of the predictive model.

A. Representation of Coherent Structures

The focus of this work is on the peak jet noise, which is widely agreed to originate from "large-scale" or "coherent" turbulent structures in the jet.[18,19] The RANS flow field, of course, is devoid of any time-resolved information that one could connect to coherent structures. To bridge this gap, we look at the main contributions of the large eddies: the transport of quantities such as momentum, heat, species, etc., across the jet. Focusing on the momentum transport, in a statistical sense the effect of turbulent eddies is captured by the velocity correlation $\overline{\mathbf{u}'\mathbf{u}'}$, where $\overline{(\,)}$ denotes the ensemble average, or the associated Reynolds stress tensor $-\overline{\rho}\overline{\mathbf{u}'\mathbf{u}'}$. The coherent structures induce the largest contributions in the Reynolds stress. The Reynolds stress itself is a key ingredient in the production of turbulence, as expressed by the evolution equation for the turbulent kinetic energy[20]

$$\frac{Dk}{Dt} \;=\; -\overline{\mathbf{u}'\mathbf{u}'} : \nabla\overline{\mathbf{u}} \;-\; \epsilon \tag{1}$$

Here D/Dt means the total derivative associated with the mean flow, $\nabla\overline{\mathbf{u}}$ is the mean velocity gradient, and ϵ is the dissipation. Even though this equation is written in a simplified form for homogeneous turbulence, it nevertheless captures the essential premise of the current work: the action of the turbulent eddies is best represented by the Reynolds stress, not the turbulent kinetic energy. The turbulent kinetic energy k is an integral effect of the production and dissipation terms in Eq. 1. It will be shown later that there are significant differences in the distributions of the Reynolds stress and turbulent kinetic energy in the jet flow field, which have a direct impact on the modeling attempted here.

In summary, the Reynolds stress will be a central element of the modeling effort. It will guide the appropriate definition of a convective Mach number, and will influence the amplitude of the space-time correlation.

B. Suppressed Communication through the Jet Flow

A central premise of the model is that the sound generated by coherent structures *in the direction of peak emission* (shallow polar angles to the jet axis) radiates mostly outward, with minimal radiation inward (through the jet flow). For a physical explanation, consider first a single-stream jet. The convective velocity of the shear-layer eddies has been measured by a number of studies to be in the range of 60% to 70% of the jet exit velocity.[21,22] As a result, the convective Mach number of the eddies relative to the ambient is larger than the convective Mach number relative to the jet flow. For exhaust conditions typical for aeroengines, the outer convective Mach number is high subsonic or supersonic, while the inner convective Mach number is low subsonic. This means high radiation efficiency (a term that will be defined in Secton II.H) for outward propagation and very low radiation efficiency for inward propagation. The sound that propagates inward and emerges from the opposite side of the jet is very weak compared to the outward-propagated sound. This concept will be generalized to a multistream jet in Section III.H.

The suppression of inward radiation is supported by measurements of the azimuthal coherence of the jet pressure field. For separation angle of 180°, and for frequencies of relevance to aircraft noise (Strouhal

numbers on the order of one or higher), the azimuthal coherence is zero.[23] If even a tiny fraction of the eddy-generated sound "leaked" through the other side of the jet, a finite coherence would be expected. In fact, the azimuthal coherence is very weak for much smaller separation angles, indicating (a) the finite azimuthal scale of the eddies and (b) the suppression of inward propagation. Finally, the suppression of inward propagation, and finiteness of the azimuthal scales, are evident by a wealth of data on the sound emission of jets with induced asymmetry (including data in this paper) which show azimuthal variations of up to 20 decibels, a factor of 100 in pressure amplitude. Such large azimuthal changes would not be possible if inward propagation were appreciable. The experimental evidence is not limited to asymmetric jets. Jets from nozzle with inserts or lobes show distinct azimuthal variations in the far-field sound.[24]

The picture becomes murkier and more complex at large polar angle to the jet axis. There, the outward radiation efficiency can be very weak, even at high convective Mach number. So, the inner and outward propagation could be of competing strengths. Indeed, experiments show that, at large polar angles, loud events on one side of the jet can increase the sound emission on the opposite side. Until a better physical understanding of sound refraction at large polar angle is developed, the arguments presented in the previous two paragraphs can only be confidently applied in or near the direction of peak emission. Accordingly, the scope of the analysis that follows is confined to the peak radiated sound.

C. Dominance of Outer Shear Layer

As a corollary to the notion of suppressed communication through the jet flow, we argue that the sound generated by the coherent structures of the outermost shear layer of the jet is not significantly effected by refraction effects. In past works refraction has been approached from the standpoint of localized sources embedded in a mean flow.[25,26] This concept is questionable as far as *outward* radiation from large-scale coherent structures is concerned. These coherent structures are in direct contact with the irrotational ambient medium, so the sound generation involves a direct coupling between the turbulent motion and the pressure field. Mean flow - acoustic interactions are deemed negligible, except in polar directions close to the angle of growth of the jet flow. We will further argue that, in multistream jets of relevance to aircraft propulsion, the outermost shear layer is the strongest contributor to peak noise. This point will be illustrated by the data of the present study.

III. Acoustic Analogy Model

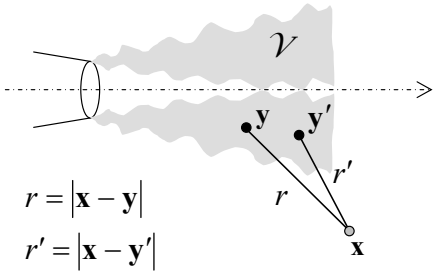

Figure 1. Setup of the Lighthill acoustic analogy model.

A. Fundamental Solution

We review briefly the Lighthill acoustic analogy,[27] emphasizing features that are salient to the present modeling effort. Referring to Fig. 1, the noise source region occupies a volume $\mathcal{V}$, locations $\mathbf{y}$ and $\mathbf{y}'$ refer to points inside the source region, and location $\mathbf{x}$ is a field point outside the source region. The distances between the field point and the source locations are $r = |\mathbf{x} - \mathbf{y}|$ and $r' = |\mathbf{x} - \mathbf{y}'|$. Through a rearrangement of the Navier-Stokes equations, the pressure fluctuation p' outside the source region can be shown to satisfy the linear inhomogeneous wave equation

$$\frac{1}{a_\infty^2}\frac{\partial^2 p'}{\partial t^2} - \frac{\partial^2 p'}{\partial x_i \partial x_i} = \frac{\partial^2 T_{ij}}{\partial y_i \partial y_j} \tag{2}$$

where a_∞ is the speed of sound of the uniform stationary medium surrounding the source and T_{ij} is the Lighthill stress tensor

$$T_{ij} = \rho u_i u_j + (p - a_\infty^2 \rho)\delta_{ij} - \tau_{ij} \tag{3}$$

where τ_{ij} denotes the viscous stress. The exact solution of Eq. 2 in 3D free space is

$$p'(\mathbf{x},t) = \frac{\partial^2}{\partial x_i \partial x_j} \int_{\mathcal{V}} T_{ij} \left(\mathbf{y},\ t - \frac{r}{a_\infty} \right) \frac{1}{4\pi r} d^3\mathbf{y} \tag{4}$$

where $1/(4\pi r)$ represents the spatial distribution of the free-space Green's function. Applying the chain rule, and neglecting terms that decay faster than the inverse first power of the distance, the double divergence is converted to a second time derivative,

$$p'(\mathbf{x},t) = \frac{1}{a_\infty^2} \int_{\mathcal{V}} \vartheta_i \vartheta_j \frac{\partial^2 T_{ij}}{\partial t^2} \left(\mathbf{y},\ t - \frac{r}{a_\infty} \right) \frac{1}{4\pi r} d^3\mathbf{y} \tag{5}$$

where

$$\vartheta_i \ = \ \frac{x_i - y_i}{r} \tag{6}$$

is the direction cosine between observer and source. Even though the derivative transformation in Eq. 5 is commonly associated with a far-field approximation, it is important to note that Eq. 5 gives the *acoustic* pressure everywhere, that is, in the near field and in the far field.[27–29] This is because the neglected terms in the transformation decay faster than r^{-1} and thus comprise the hydrodynamic pressure.

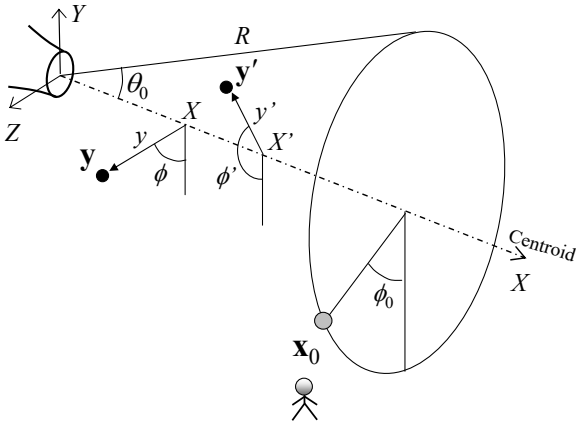

Figure 2. Coordinate systems.

B. Spectral Density

The autocorrelation of the pressure at observer location $\mathbf{x}_0$ is

$$\begin{aligned} \overline{p'(\mathbf{x}_0,t)p'(\mathbf{x}_0,t+\tau)} \ &= \frac{1}{16\pi^2 a_\infty^4} \int_{\mathcal{V}} \int_{\mathcal{V}} [\vartheta_i \vartheta_j \vartheta'_k \vartheta'_l]_0 \\ &\times \ \overline{\frac{\partial^2 T_{ij}(\mathbf{y}, t - r_0/a_\infty)}{\partial t^2} \frac{\partial^2 T_{kl}(\mathbf{y}', t + \tau - r'_0/a_\infty)}{\partial t^2}} \frac{1}{r_0 r'_0} d^3\mathbf{y}' d^3\mathbf{y} \end{aligned} \tag{7}$$

Here $\overline{(\ )}$ denotes the expectation or ensemble average, $r_0 = |\mathbf{x} - \mathbf{y}|$, and $r'_0 = |\mathbf{x}_0 - \mathbf{y}'|$. We assume stationarity in time and define accordingly the space-time correlation of the Lighthill stress tensor as

$$R_{ijkl}(\mathbf{y}, \mathbf{y}', \tau) \ = \ \overline{T_{ij}(\mathbf{y}, t) T_{kl}(\mathbf{y}', t + \tau)} \tag{8}$$

The stationarity allows us to take the time differentiation outside the correlation of Eq. 7, writing it as $\partial^4/\partial\tau^4\overline{(\ )}$ (see p. 317 of Ref. 30). In addition, it enables the time shift $t - r_0/a_\infty \to t$. These steps result in

$$\overline{p'(\mathbf{x}_0,t)p'(\mathbf{x}_0,t+\tau)} = \frac{1}{16\pi^2 a_\infty^4}\int_{\mathcal{V}}\int_{\mathcal{V}}[\vartheta_i\vartheta_j\vartheta'_k\vartheta'_l]_0\frac{\partial^4}{\partial\tau^4}R_{ijkl}\left(\mathbf{y},\mathbf{y}',\tau+\frac{r_0-r'_0}{a_\infty}\right)\frac{1}{r_0 r'_0}d^3\mathbf{y}'d^3\mathbf{y} \tag{9}$$

The spectral density is the Fourier transform of the autocorrelation,

$$S(\mathbf{x}_0,\omega) \;=\; \int_{-\infty}^{\infty}\overline{p'(\mathbf{x}_0,t)p'(\mathbf{x}_0,t+\tau)}\;e^{-i\omega\tau}d\tau \tag{10}$$

Using Eq. 9,

$$S(\mathbf{x}_0,\omega) = \frac{\alpha^4}{16\pi^2}\int_{\mathcal{V}}\int_{\mathcal{V}}\int_{-\infty}^{\infty}[\vartheta_i\vartheta_j\vartheta'_k\vartheta'_l]_0 R_{ijkl}(\mathbf{y},\mathbf{y}',\tau)\frac{\exp\left[i\alpha(r_0-r'_0)-i\omega\tau\right]}{r_0 r'_0}d\tau d^3\mathbf{y}'d^3\mathbf{y} \tag{11}$$

Equation 11 gives the *acoustic* component of the spectral density everywhere. At this point the only assumption is the stationarity in time of the flow statistics.

C. Coordinate System

The study of azimuthal effects necessitates the use of a cylindrical polar coordinate system in the implementation of Eq. 11. The complexity of the problem requires the inclusion of Cartesian and spherical coordinates. The three coordinate systems used here are illustrated in Fig. 2: Cartesian (X,Y,Z); cylindrical polar (X,y,ϕ); and spherical (R,θ,ϕ). The Cartesian coordinate system will also described by indices 1 (X), 2 (Y), and 3 (Z), with the index 23 referring to combined properties on the cross-stream $(Y-Z)$ plane. Index 4 will refer to time.

Selection of an appropriate jet axis, on which the definitions of radial distance y and azimuthal angle ϕ are based, is critical for capturing the azimuthal effects on noise emission. In this regard, the nozzle axis is a poor choice because asymmetric jets have distorted mean velocity profiles and could be vectored upward or downward. In Section III.F the Lighthill stress tensor will be connected to the Reynolds stress, whose dominant component scales with the magnitude of the mean velocity gradient

$$G \;=\; |\nabla\overline{\mathbf{u}}| \tag{12}$$

The decision then is to define the center of the jet as the point where Reynolds stress vanishes, or $G=0$, within the jet flow. This definition is straightforward for the region past the end of the primary potential core, where the profile of the mean flow is Gaussian-like. There, the location of $G=0$ coincides with the location of the maximum mean velocity $\overline{u}_{max}$. For the region of the jet comprising the primary potential core, the locations of $G=0$ or $\overline{u}_{max}$ are ill-defined. However, one can calculate fairly reliably the centroid of the high-speed region, defined by a criterion like $\overline{u} > 0.9\overline{u}_{max}$. In fact, this criterion can be extended to the region past the end of the primary potential core where, for noisy experimental or numerical data, it provides a more reliable estimate of the location of $\overline{u}_{max}$. Accordingly, for a given axial station $X = X_1$ we identify the region of high-speed flow using the criterion

$$\overline{u}(X_1,Y,Z) > 0.9\;\overline{u}_{max}(X_1)$$

Denoting Y_i, $i=1,\ldots,N$, the Y locations at which this criterion is satisfied, the jet centroid is computed according to

$$Y_c(X_1) \;=\; \frac{1}{N}\sum_{i=1}^{N}Y_i \tag{13}$$

Then the $Y-$coordinates of all the data points at this axial station are decremented by Y_c, so that $Y=0$ becomes the centroid location. This process is applied to all the axial stations within the computational domain.

D. Far Field Approximation

The far-field version of Eq. 11 is now developed, using the coordinate systems depicted in Fig. 2. The source locations are described in cylindrical polar coordinates

$$\mathbf{y} = (X, y, \phi) \quad , \quad \mathbf{y}' = (X', y', \phi')$$

In the spherical coordinate system, the observer is situated at

$$\mathbf{x}_0 \ = (R, \theta_0, \phi_0)$$

For $R >> \ell$, where ℓ is a characteristic dimension of the source, $\vartheta_i \approx \vartheta_i' \approx x_i/R$ and $1/(r_0 r_0') \approx 1/R^2$. Further,

$$r_0 - r_0' \ \approx \ (X' - X)\cos\theta_0 \ + \ \sin\theta_0 \left[y' \cos(\phi' - \phi_0) - y\cos(\phi - \phi_0)\right] \tag{14}$$

Although the axial source separation $X' - X$ readily appears on the right hand side, the radial and azimuthal separations are interconnected and cannot be separated cleanly into distinct terms. This is an important consequence of using the polar-cylindrical coordinate system to express the source location; it will prevent the formulation of the spectral density as a four-dimensional Fourier transform of the space-time correlation, a common procedure in past treatments of the acoustic analogy.[11,31]

On defining the projection of R_{ijkl} along the observer direction as

$$R_{0000}(\mathbf{y}, \mathbf{y}', \tau) \ = \ [\vartheta_i \vartheta_j \ \vartheta_k \vartheta_l]_0 \ R_{ijkl}(\mathbf{y}, \mathbf{y}', \tau) \tag{15}$$

the spectral density for the far-field observer becomes

$$\begin{aligned} S(\mathbf{x}_0, \omega) \ = \ & \frac{\alpha^4}{16\pi^2 R^2} \int_{\mathcal{V}} \int_{-\pi}^{\pi} \int_0^{\infty} \int_0^{\infty} \int_{-\infty}^{\infty} R_{0000}(\mathbf{y}, \mathbf{y}', \tau) \\ & \times \exp(i\alpha \cos\theta_0 (X' - X) - i\omega\tau) \\ & \times \exp\left\{i\alpha \sin\theta_0 \left[y' \cos(\phi' - \phi_0) - y\cos(\phi - \phi_0)\right]\right\} d\tau \ dX' \ y' dy' \ d\phi' \ d^3\mathbf{y} \end{aligned} \tag{16}$$

In Eq. 16 the integrals over the shifted space and time coordinates are shown explicitly, while the integration over the source volume $\mathcal{V}$ is displayed compactly. The spatial coordinates in the exponent arise from the free-space Green's function in the frequency domain.

E. Model for the Space-Time Correlation

The space-time correlation model used here is defined in a fixed frame of reference. It is guided by experimental measurements of space-time correlations in the flow or near acoustic field of turbulent jets,[21–23,29] with important simplifications and modifications. Figure 3 sketches the typical shape of the axial space-time correlation of a fluctuating quantity (velocity, velocity squared, pressure, etc.) The evolution of the timewise correlation R_4 reflects the convection of turbulence with a velocity U_c and its decorrelation with increasing axial separation $|X' - X|$. At zero spatial separation, R_4 is the autocorrelation and decays roughly exponentially with the time separation τ. With increasing $|X' - X|$, the timewise correlation peaks at $\tau = (X' - X)/U_c$ and is modulated by the axial correlation $R_1(X' - X)$; in addition, the shape of R_4 broadens and becomes more Gaussian-like. Negative loops are evident throughout the evolution of R_4. For finite axial separation, the space-time correlation is not symmetric around $\tau = 0$, reflecting the non-stationarity of spatial statistics and the associated increase of length and time scales with downstream distance.

Having noted the principal features of the axial space-time correlation, we outline the simplifications and modifications implemented here. The timewise and axial correlations will be treated as symmetric functions, thus neglecting the effects of spatial non-stationarity. The timewise correlation R_4 will be invariant with axial separation and will include a transverse propagation time, in addition to the axial propagation time noted above. In the transverse dimensions of the problem, we will employ a mixed correlation R_{23} whose precise form will be the subject of detailed analysis. The resulting correlation has the form

$$R_{ijkl}(\mathbf{y}, \mathbf{y}', \tau) \ = A_{ijkl}(\mathbf{y}) \ R_1\Big(\frac{X' - X}{L_1(\mathbf{y})}\Big) R_{23}\Big(y, y', \phi, \phi', L_{23}(\mathbf{y})\Big) R_4 \left(\frac{\tau - \dfrac{X' - X}{U_c(\mathbf{y})} - \dfrac{d}{V_c(\mathbf{y})}}{\tau_*(\mathbf{y})} \right) \tag{17}$$

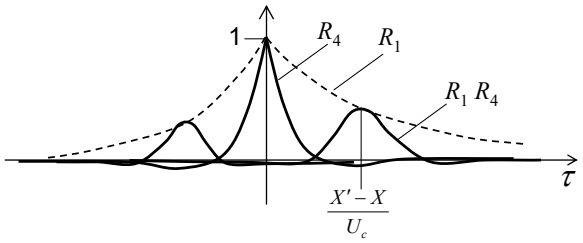

Figure 3. Illustration of the typical shape of the axial space-time correlation.

Here A_{ijkl} is the amplitude of the correlation; R_1 and R_4 are the axial and timewise correlations, respectively; R_{23} is a mixed radial/azimuthal correlation; L_1 and L_{23} and are the correlation length scales in the axial and transverse directions, respectively; and τ_* is the correlation time scale. The timewise correlation R_4 includes axial and transverse propagation times. The axial propagation time $(X'-X)/U_c$ is connected to the streamwise eddy convection at velocity U_c. The transverse propagation time d/V_c is a special construct that will be shown to induce azimuthal directivity in the emission of the sound. It is based on a transverse distance d and a transverse propagation velocity V_c. The axial and transverse convective Mach numbers are $M_c = U_c/a_\infty$ and $\mu_c = V_c/a_\infty$, respectively. Equation 17 shows explicitly the dependence of the amplitude and scales on the source location $\mathbf{y}$. This notation will be henceforth dropped to reduce clutter.

The notion of a transverse propagation time scale can be found in the works of Harper-Bourne[29] and Raizada and Morris.[32] In this study, the concept should not be seen as anything more than a mathematical construct to induce azimuthal influence, as will be demonstrated in the analysis of Section III.E. Nevertheless, it is helpful to have some insight as to the physical meaning of V_c. Consider two points at the same axial location but separated laterally. If the turbulence is highly uncorrelated spatially, so that the correlation scale is much smaller than the separation of the two points, the speed at which a disturbance propagates from the first point to the second point cannot exceed the local acoustic velocity. On the other hand, if the turbulence convects downstream in highly organized pattern whose correlation scale is much larger than the separation of the two points, then a disturbance at one point is felt instantly at the other point, resulting in an infinite lateral propagation speed. In the uncorrelated case, a transverse convective Mach number on the order of 1 ($\mu_c \sim 1$) represents an upper bound. In the strongly correlated case, $\mu_c \to \infty$ and the transverse term drops out from the argument of R_4.

1. *Generic Shape for the Correlations*

The correlation shapes employed here fall under the class of the "stretched exponential"

$$R_j(t) \;=\; e^{-|t|^{\beta_j}}, \tag{18}$$

also called the Kohlrausch function.[33] The flexibility provided by this function will be used in the axial ($j=1$) and timewise ($j=4$) dimensions, where the range $0.7 \le \beta_j \le 2$ will be allowed. On the transverse plane ($j=23$) only the integer values $\beta_{23}=1$ and 2 will be considered for the sake of numerical efficiency.

Since R_j is an even function, its Fourier transform is real and equal to twice the cosine transform:

$$\widehat{R}_j(\eta) \;=\; 2\int_0^\infty R_j(t)\cos(\eta t)dt \tag{19}$$

Note that $\widehat{R}_j$ assumes the analytical forms

$$\widehat{R}_j(\eta) \;=\; \frac{2}{1+\eta^2} \quad , \quad \beta_j = 1$$

$$\widehat{R}_j(\eta) \;=\; \sqrt{\pi}e^{-\frac{1}{4}\eta^2} \quad , \quad \beta_j = 2$$

For powers β_j other than 1 (exponential) or 2 (Gaussian) the Fourier transform does not have an analytical expression and needs to be calculated numerically. For computational efficiency, the transform $\widehat{R}_j(\eta)$ was

computed once and was tabulated versus η and β_j; subsequent operations used two-dimensional interpolation of the table. Great care is required in evaluating near $\beta_j = 2$ where the shape of the Fourier transform is extremely sensitive on $2 - \beta_j$.

The stretched exponential will be used here with a reference scale, that is, $R_j(t) = \exp(-|t/\tau|^{\beta_j})$. Its Fourier transform is simply $\tau\widehat{R}_j(\tau\eta)$. Evaluated at $\eta = 0$, it gives the integral scale $\tau\widehat{R}_j(0)$. It can be shown that

$$\widehat{R}_j(0) = \frac{1}{\beta_j}\,\Gamma\left(\frac{1}{\beta_j}\right) \tag{20}$$

where Γ is the Gamma function.[33] For $0.7 \le \beta_j \le 2$, the corresponding range for $\widehat{R}_j(0)$ is $1.266 \ge \widehat{R}_j(0) \ge 0.886$. Thus, the integral scale is not too different from the reference scale.

Figure 4 illustrates the behavior of the stretched exponential and its transform for $0.7 \le \beta_j \le 2$, the range allowed in this study. For clarity the transform is shown in decibels. The sensitivity of the transform on the power β is apparent and represents a key ingredient of the optimization process employed here. For the selected range of β_j, the Fourier transform is non-negative for all frequencies.

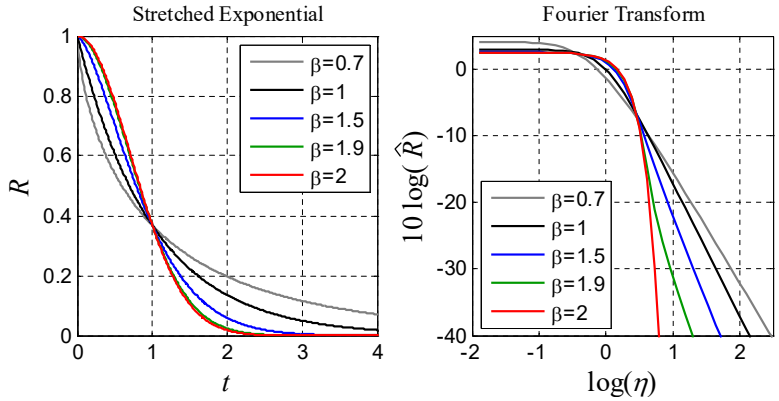

Figure 4. Correlation function (a) and its Fourier transformation (b) for various values of β.

2. *Axial and Timewise Fourier Transforms*

The timewise integration in Eq. 16 amounts to a Fourier transform in the time separation τ. Given the slow axial development of the flow, the X' integral can be approximated as an integral over the axial separation $X' - X$ ranging from $-\infty$ to ∞, and thus can also be treated as a Fourier transform in $X' - X$. This assumes that the scale of the axial correlation is much smaller than the distances X or X' and neglects the fact that both X and X' have a finite origin at zero. Fourier transforms in the transverse dimensions of the problem are not appropriate. As indicated in the discussion of Eq. 14, the radial and azimuthal components of the Green's function cannot be expressed in terms of separations $y' - y$ and $\phi' - \phi$. Even if one were to overlook this fact, the concept of a Fourier transform in the radial separation $y' - y$ breaks down because of the rapid evolution of the flow in the radial direction: the radial correlation scale cannot be considered small compared to either y' or y. Finally, the azimuthal periodicity of the correlation prevents the writing of the $d\phi'$ integral as a Fourier transform.

We conclude that Fourier transformation is only possible in the timewise and axial directions; the procedure is rigorous in the timewise dimension and acceptable as an approximation in the axial dimension. Inserting the correlation form of Eq. 17 in Eq. 16, and carrying out the Fourier transforms in τ and $X' - X$, we obtain

$$\begin{aligned} S(\mathbf{x}_0,\omega) = {} & \frac{\alpha^4}{16\pi^2 R^2}\int_{\mathcal{V}} A_{0000}\tau_* L_1\ \widehat{R}_1\left[\alpha L_1\left(\frac{1}{M_c}-\cos\theta_0\right)\right]\ \widehat{R}_4\left[\omega\tau_*\right]\ \exp\left(-i\,\frac{\alpha d}{\mu_c}\right) \\ & \times\int_{-\pi}^{\pi}\int_{0}^{\infty} R_{23}\exp\left\{i\alpha\sin\theta_0\left[y'\cos(\phi'-\phi_0)-y\cos(\phi-\phi_0)\right]\right\}\ y'dy'\ d\phi'\ d^3\mathbf{y} \end{aligned} \tag{21}$$

Omitting the arguments, we write this compactly as

$$S(\mathbf{x}_0,\omega) \;=\; \frac{\alpha^4}{16\pi^2 R^2}\int_{\mathcal{V}} A_{0000}\;\tau_* L_1 \pi L_{23}^2\;\widehat{R}_1\widehat{R}_4\widetilde{R}_{23}\;d^3\mathbf{y} \tag{22}$$

where

$$\widetilde{R}_{23} \;=\; \frac{1}{\pi L_{23}^2}\int_{-\pi}^{\pi}\int_0^{\infty} R_{23}(y,y',\phi,\phi')\exp\left\{i\alpha\sin\theta_0\left[y'\cos(\phi'-\phi_0)-y\cos(\phi-\phi_0)\right]-i\alpha\frac{d}{\mu_c}\right\}\;y'dy'\;d\phi' \tag{23}$$

In Eq. 22 the term πL_{23}^2 represents a cross-stream correlation area, and the product $\tau_* L_1 \pi L_{23}^2$ can be viewed as a four-dimensional correlation "volume". As discussed in Section III.E.1, the functions $\widehat{R}_1$ and $\widehat{R}_4$ are real and non-negative. The meaning and behavior of $\widetilde{R}_{23}$ will be the topic of the discussion that follows.

3. Cross-Stream Correlation

As noted in Section III.E.2, the transverse correlation R_{23} is not amenable to Fourier transforms. Instead, the spectral transformation of R_{23} takes the form of the integral of Eq. 23. Evaluation of this integral, and determination of allowable forms for R_{23} and the separation distance d, are governed by the requirement that the power spectral density $S(\mathbf{x}_0,\omega)$, given by Eq. 22, be real and non-negative. To satisfy this requirement for an arbitrary source distribution, $\widetilde{R}_{23}$ must be real and non-negative (recall that $\widehat{R}_1$ and $\widehat{R}_4$ are real and non-negative for the class of correlation functions selected here). A further requirement is that R_{23} be periodic in the azimuthal separation $\phi'-\phi$.

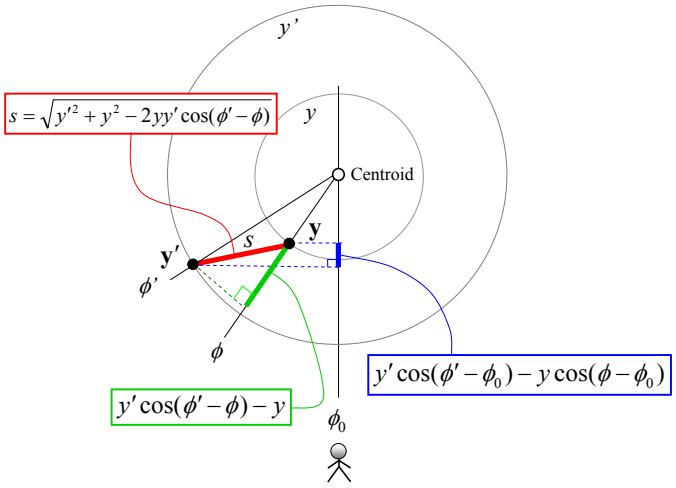

Figure 5. Geometric relations on the cross-stream plane.

Equation 23 entails integration over the cross-stream plane. Its evaluation is facilitated by examining key geometric relations on this plane. Figure 5 depicts the projections of source elements $\mathbf{y}$ and $\mathbf{y}'$ and the resulting geometric relations on the cross-stream plane, with the observer located at azimuthal angle ϕ_0. All the distances discussed here will be *projected* distances on the cross-stream plane. The distance between elements $\mathbf{y}$ and $\mathbf{y}'$ is

$$s=\sqrt{y'^2+y^2-2yy'\cos(\phi'-\phi)} \tag{24}$$

and the projection of this distance on the observer radial line is $y'\cos(\phi'-\phi_0)-y\cos(\phi-\phi_0)$. This is precisely the term that appears in the exponent of Eq. 23. It thus becomes evident that a coordinate system centered at the source location $\mathbf{y}$, rather than at the centroid, is preferred for evaluating Eq. 23. Accordingly, the origin is shifted from the centroid to the location of source element $\mathbf{y}$, as shown in Fig. 6. All the azimuthal angles are now defined with respect to the observer angle ϕ_0. The observer being in the far field, the coordinate shift does not change the angular relations. In the new coordinate system, the

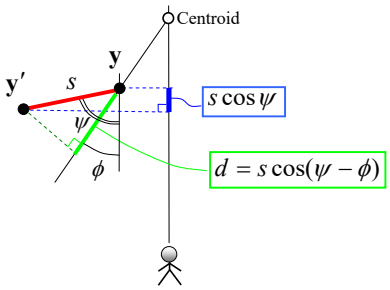

Figure 6. Geometric relations in shifted coordinate system on the cross-stream plane. Without loss of generality, the observer is placed at $\phi_0 = 0$.

azimuthal angle of element $\mathbf{y}'$ is ψ. The term $y'\cos(\phi' - \phi_0) - y\cos(\phi - \phi_0)$ reduces to $s\cos\psi$. Changing the integration variables from (y', ϕ') to (s, ψ) we obtain

$$\begin{aligned} \widetilde{R}_{23} &= \frac{1}{\pi L_{23}^2}\int_{-\pi}^{\pi}\int_0^{\infty} R_{23} e^{i\gamma s\cos\psi - i\delta d}\; sds\; d\psi \\ \gamma &= \alpha\sin\theta_0 \\ \delta &= \alpha/\mu_c \end{aligned} \tag{25}$$

Although an exhaustive treatise of this integral is beyond the scope of the current work, a straightforward strategy for satisfying the requirement of real non-negativeness will be set forth by invoking the integral representation of the Bessel function of the first kind and of order zero:

$$2\pi J_0(x) = \int_{-\pi}^{\pi} e^{ix\cos\psi}\; d\psi$$

First, if d is related to s through a projection of the type $d = s\cos(\psi - \chi)$, where χ is a reference angle, integration over ψ yields $2\pi J_0(\zeta s)$, where ζ is a real positive number. Then, on selecting $R_{23} = R_{23}(s)$, the integral over s becomes the Hankel transform of R_{23}. Here the natural choice for d is

$$d = s\cos(\psi - \phi) = y'\cos(\phi' - \phi) - y, \tag{26}$$

that is, d is the projection of s on the radial ϕ. Integration over ψ results in a Bessel function, and Eq. 23 becomes

$$\widetilde{R}_{23} = \frac{2}{L_{23}^2}\int_0^{\infty} R_{23}(s)\; J_0\left(s\sqrt{\gamma^2 + \delta^2 - 2\gamma\delta\cos(\phi - \phi_0)}\right)\; sds \tag{27}$$

yielding the Hankel transform of $R_{23}(s)$. We seek forms for $R_{23}(s)$ that result in analytical, non-negative solutions. Exponential and Gaussian kernels satisfy these conditions.[34] Accordingly, we select

$$R_{23} = \exp\left[-\left(\frac{s}{L_{23}}\right)^{\beta_{23}}\right] \tag{28}$$

and restrict $\beta_{23} = 1$ or 2. Evaluation of the Hankel transform gives

$$\begin{aligned} \widetilde{R}_{23} &= \left\{1 + \left(\frac{\alpha L_{23}}{2}\right)^2\left[\sin^2\theta_0 + \frac{1}{\mu_c^2} - 2\frac{\sin\theta_0}{\mu_c}\cos(\phi - \phi_0)\right]\right\}^{-3/2}, \qquad \beta_{23} = 1 \\ \widetilde{R}_{23} &= \exp\left\{-\left(\frac{\alpha L_{23}}{2}\right)^2\left[\sin^2\theta_0 + \frac{1}{\mu_c^2} - 2\frac{\sin\theta_0}{\mu_c}\cos(\phi - \phi_0)\right]\right\}, \qquad \beta_{23} = 2 \end{aligned} \tag{29}$$

Therefore we satisfy the requirement for a real non-negative spectral density. Note that R_{23} is periodic with the azimuthal separation $\phi' - \phi$, as is readily observed by inserting Eq. 24 in Eq. 28. Importantly, the term

$\cos(\phi - \phi_0)$ in Eq. 29 induces an azimuthal influence that is central for simulating the effect of suppressed communication through the jet flow discussed in Section II.B.

Even though the selection for $R_{23}(s)$ can encompass functions that do not have analytical Hankel transforms (similar to the treatment of non-analytical Fourier transforms in Section III.E.1), the desire for analytical forms stems from numerical considerations in evaluating the spectral density of the reference (axisymmetric) jet. As will be discussed in Section III.G.3, analytical solutions for $\widetilde{R}_{23}$ enable very efficient evaluation of the reference spectral density, a critical feature of the predictive model. Non-analytical solutions would largely preclude such efficiency, although some computational savings could arise from the use of look-up tables coupled with sophisticated interpolation schemes.

4. Azimuthal Influence

We examine the azimuthal directivity of $\widetilde{R}_{23}$, selecting the case $\beta_{23} = 2$ in Eq. 29. The case with $\beta_{23} = 1$ would follow a similar treatment. The azimuthal directivity arises from the term $\cos(\phi - \phi_0)$ and is directly controlled by the transverse convective Mach number μ_c. For $\mu_c = \infty$, $\widetilde{R}_{23}$ does not have an azimuthal variation. For μ_c finite and positive, the azimuthal influence has an extent that is controlled by μ_c and by the transverse non-dimensional wave number αL_{23}. Figure 7 illustrates these dependencies for observer polar angle $\theta_0 = 30°$. At fixed αL_{23}, the strongest azimuthal directivity is obtained for $\mu_c = 1/\sin\theta_0$ ($\mu_c = 2$ in this example). At fixed μ_c, the directivity sharpens with increasing αL_{23} (increasing frequency).

The observations would tempt one to set $\mu_c = 1/\sin\theta_0$ to maximize the azimuthal influence. Of course, this is not a legitimate step because the correlation parameters should be independent of observer location. The approach in this study is to set

$$\mu_c \;=\; \frac{1}{\sin\theta_{peak}}$$

where θ_{peak} is the angle of peak emission, in terms of overall sound pressure level, for the baseline axisymmetric jet. The combined influence of μ_c and L_{23} on the azimuthal influence places some constraints on the transverse correlation scale L_{23}. Specifically, a lower constraint should be placed on the coefficient that controls L_{23} such that, at given frequency, αL_{23} is not too small.

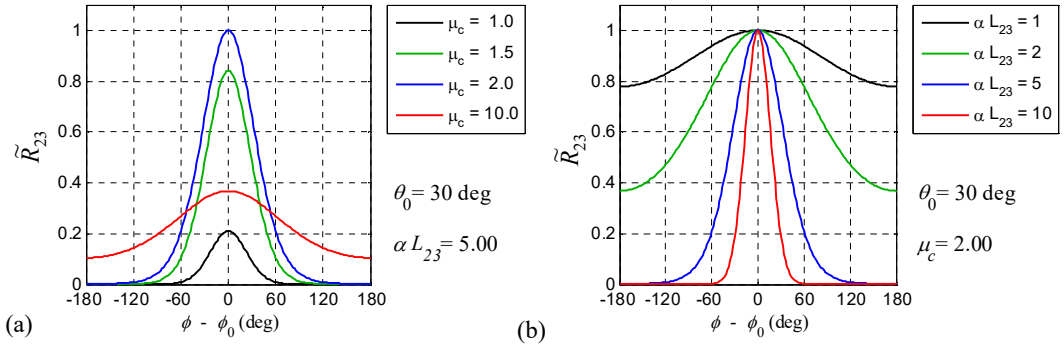

Figure 7. Azimuthal distribution of $\widetilde{R}_{23}$ for observer polar angle $\theta_0 = 30$ deg. (a) Fixed αL_{23} and varying μ_c; (b) fixed μ_c and varying αL_{23}.

The present model for μ_c is selected for its simplicity. More sophisticated models, where μ_c depends on flow conditions and frequency, may provide higher levels of fidelity.

F. Amplitude of the Correlation

The amplitude A_{ijkl} in Eq. 17 represents the correlation

$$R_{ijkl}(\mathbf{y}, \mathbf{y}, 0) \;=\; \overline{T_{ij}(\mathbf{y}, t) T_{kl}(\mathbf{y}, t)} \tag{30}$$

It is important to recall, however, that the source term in Eq. 9 is not R_{ijkl} itself but $\partial^4 R_{ijkl}/\partial\tau^4$. This means that only terms that depend on τ can make a contribution towards A_{ijkl}. It is thus convenient to

express A_{ijkl} as

$$A_{ijkl}(\mathbf{y}) \;=\; \overline{[T_{ij}]_a[T_{kl}]_b}, \quad a \to b \tag{31}$$

where a and b represent different times. Only correlations that involve both a and b are to be retained.

We assume that the principal component of the Lighthill stress tensor is $T_{ij} = \overline{\rho} u_i u_j$ and write the velocity components as

$$\begin{aligned} u_1 &= \overline{u} + u' \\ u_2 &= v' \\ u_3 &= w' \end{aligned} \tag{32}$$

where u', v', w' are the fluctuating velocity components in Cartesian coordinates. The distinct Lighthill tensor components are

$$\begin{aligned} T_{11} &= \overline{\rho}(\overline{u}^2 + 2\overline{u}u' + u'u') \\ T_{12} &= \overline{\rho}(\overline{u}v' + u'v') \\ T_{13} &= \overline{\rho}(\overline{u}w' + u'w') \\ T_{22} &= \overline{\rho}v'v' \\ T_{23} &= \overline{\rho}v'w' \\ T_{33} &= \overline{\rho}w'w' \end{aligned} \tag{33}$$

Following the rule accompanying Eq. 31, only cross-terms like $\overline{u'_a v'_b}$ will be retained; terms like $\overline{u'_a v'_a}$ do not contribute to the source. Under the assumption of isotropic turbulence, the volume integral of the third-order correlations vanishes.[35] Although the validity of this assumption needs to be evaluated thoroughly, here we will neglect third-order correlations like $\overline{u'_a v'^2_b}$. The resulting evaluation of A_{ijkl} leads to terms containing second-order correlations $\overline{u'_i u'_j}$, usually referred to as "shear noise"; and terms containing fourth-order correlations $\overline{u'_i u'_j u'_k u'_l}$, typically described as "self noise". A preliminary evaluation of the self-noise terms, using the quasi-normal hypothesis[22] and the approximations that follow, indicates that their contribution to peak noise is at least 10 dB below the contribution of the shear-noise terms. Therefore, the fourth-order correlations are deemed irrelevant to the prediction of peak noise.

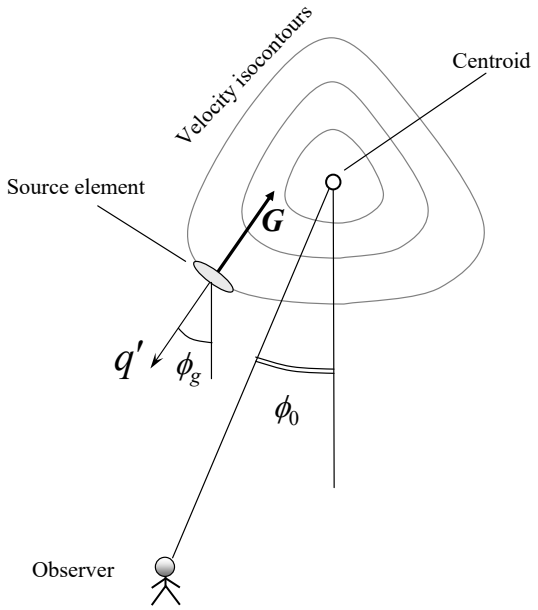

Figure 8. Azimuthal relationships of source and observer.

Thus, the problem boils down to modeling the second-order correlations, that is, the components of the Reynolds stress tensor. To this end, we use the constitutive relation that forms the foundation of turbulence

modeling[20]

$$\overline{u_i' u_j'} \;=\; \frac{2}{3}k\delta_{ij} - \nu_T S_{ij} \tag{34}$$

where ν_T is the turbulent viscosity and

$$S_{ij} \;=\; \frac{\partial \overline{u}_i}{\partial x_j} + \frac{\partial \overline{u}_j}{\partial x_i} \tag{35}$$

Given that the jet flow is slowly diverging, the dominant component of S_{ij} is the transverse gradient of the mean axial velocity. The approximate magnitude of this gradient is

$$G \;=\; \sqrt{\left[\frac{\partial \overline{u}}{\partial Y}\right]^2 + \left[\frac{\partial \overline{u}}{\partial Z}\right]^2} \tag{36}$$

and its azimuthal direction is ϕ_g. Figure 8 describes the azimuthal relations between source and observer. The convention here is to assign an outward azimuthal direction for an inward gradient, and vice-versa. For an axisymmetric jet with monotonically declining radial velocity profile (that is, without a wake component), ϕ_g coincides with the geometric azimuthal angle ϕ. For a jet whose velocity isocontours are not circular, or that has a wake defect, ϕ_g and ϕ will generally be different.

It is now argued that the principal turbulent transport is in the direction of the mean flow gradient with an associated turbulent velocity fluctuation q'. The corresponding velocity correlation

$$g \;=< u'q' > =\; \nu_T G \tag{37}$$

is deemed the dominant contributor to the transport and hence to the Reynolds stress. The transport normal to the direction of the mean flow gradient is considered negligible. The correlation g will henceforth be loosely referred to as the "Reynolds stress" and will be treated as non-negative. The direction of the mean flow gradient, and its impact on the individual terms of the Reynolds stress tensor, will be accounted for by the angle ϕ_g. Returning to the constitutive relation of Eq. 34, using $v' = -q' \cos\phi_g$ and $w' = q' \sin\phi_g$, we are now able to make the following approximations:

$$\begin{aligned}
\overline{u'u'} \;&\approx\; \frac{2}{3}k \\
\overline{v'v'} \;&\approx\; \frac{2}{3}k \\
\overline{w'w'} \;&\approx\; \frac{2}{3}k \\
\overline{u'v'} \;&=\; -< u'q' > \cos\phi_g \;\approx\; -g\cos\phi_g \\
\overline{u'w'} \;&=< u'q' > \sin\phi_g \;\approx\; g\sin\phi_g \\
\overline{v'w'} \;&\approx\; 0
\end{aligned} \tag{38}$$

It is recognized that in the actual jet the axial velocity fluctuations are stronger than the transverse fluctuations, as measured by a variety of experiments (for example, Ref. citenmorris10). However, here it is preferred to stay faithful to the constitutive relation of Eq. 34.

Based on the convention of Fig. 2, the direction cosines for the far field observer are

$$\begin{aligned}
\vartheta_1 \;&=\; \cos\theta_0 \\
\vartheta_2 \;&=\; -\sin\theta_0 \;\cos\phi_0 \\
\vartheta_3 \;&=\; \sin\theta_0 \;\sin\phi_0
\end{aligned} \tag{39}$$

Due to the symmetry of T_{ij} and the resulting pairwise symmetry of A_{ijkl} (that is, $A_{ijkl} = A_{klij}$), the 81 elements of A_{ijkl} comprise single or multiple occurrences of 21 distinct terms. Of those, only 6 terms have the potential to contribute to shear noise; these are the terms where the index 1 appears at least once in ij and at least once in kl. Table 1 lists the shear-noise terms, their multipliers (frequencies), their expressions according to Eq. 33, their approximations according to Eq. 38, and their directivities according to Eq. 39.

Table 1 Distinct shear-noise terms of A_{ijkl} and associated directivities

		Expression	Approximation	
A_{ijkl}	Mult.	$\frac{A_{ijkl}}{\overline{\rho}^2\overline{u}^2}$	$\frac{A_{ijkl}}{\overline{\rho}^2\overline{u}^2}$	Directivity $\vartheta_i\vartheta_j\vartheta_k\vartheta_l$
A_{1111}	1	$4\overline{u'u'}$	$\frac{8}{3}k$	$\cos^4\theta_0$
A_{1112}	4	$2\overline{u'v'}$	$-2g\cos\phi_g$	$-\cos^3\theta_0\sin\theta_0\cos\phi_0$
A_{1113}	4	$2\overline{u'w'}$	$2g\sin\phi_g$	$\cos^3\theta_0\sin\theta_0\sin\phi_0$
A_{1212}	4	$\overline{v'v'}$	$\frac{2}{3}k$	$\frac{1}{4}\sin^2(2\theta_0)\cos^2\phi_0$
A_{1213}	8	$\overline{v'w'}$	0	$-\frac{1}{8}\sin^2(2\theta_0)\sin(2\phi_0)$
A_{1313}	4	$\overline{w'w'}$	$\frac{2}{3}k$	$\frac{1}{4}\sin^2(2\theta_0)\sin^2\phi_0$

The total contribution in the direction of the far-field observer is

$$\frac{A_{0000}}{\overline{\rho}^2\overline{u}^2} \;=\; \frac{8}{3}k\;\cos^2\theta_0 \;+\; 8g\;\cos^3\theta_0\sin\theta_0\cos(\phi_g-\phi_0) \tag{40}$$

Note that the second term on the right hand side arises from the 1112 and 1113 components of the Lighthill stress tensor. In past works on axisymmetric jets, these components were neglected because they were thought to integrate to zero when inserted in the formula for the spectral density.[35] This is not the case if we accept that the space-time correlation induces an azimuthal directivity along the lines of Eq. 29. Then, the second term of Eq. 40 does not integrate to zero and makes a finite (positive) contribution to the spectral density. Of course, the components A_{1112} and A_{1113} must be retained for asymmetric jets regardless of the chosen form of the space-time correlation.

G. Computational Considerations

Efficient computation of the power spectral density is important for the development of practical predictive tools. Efficiency is particularly desirable for the baseline, axisymmetric jets that will be subject to optimization routines requiring computation of the power spectral density a large number of times.

1. *General Relations*

Combining Eqs. 22 and 40, we express the spectral density as the following set of equations:

$$S(\mathbf{x}_0,\omega) \;=\; \int_{\mathcal{V}}\left[Q_0+Q_1\cos(\phi_g-\phi_0)\right]\;H\;d^3\mathbf{y} \tag{41a}$$

$$Q_0 \;=\; \frac{8}{3}\overline{\rho}^2\overline{u}^2k\cos^2\theta_0 \tag{41b}$$

$$Q_1 \;=\; 8\overline{\rho}^2\overline{u}^2g\cos^3\theta_0\sin\theta_0 \tag{41c}$$

$$H \;=\; \frac{\alpha^4}{16\pi R^2}\;\tau_*L_1\pi L_{23}^2\;\widehat{R}_1\widehat{R}_4\widetilde{R}_{23} \tag{41d}$$

2. *Treatment of Half Jet*

Time-averaged computations of jet flows having a plane of symmetry typically treat only one half of the jet. In these cases, it is important to be able to compute the power spectral density based on the half-jet data, that is, without creating the mirror image and thus doubling the computational cost. Even for computations that treat the entire jet, the ability to compute the power spectral density using only the symmetric half of the data provides important computational savings.

Focusing on the azimuthal component of the integration of Eq. 41a, and showing only the azimuthal dependence of the variables involved, we examine the treatment of the integral

$$I_\phi = \;\int_{-\pi}^{\pi}\Big[Q_0(\phi)+Q_1(\phi)\cos(\phi_g(\phi)-\phi_0)\Big]\;H(\phi,\phi-\phi_0)\;d\phi \tag{42}$$

For the source term H, the notation $H(\phi, \phi - \phi_0)$ indicates the azimuthal dependence of the scales as well as the azimuthal directivity of $\widetilde{R}_{23}$ that involves the term $\cos(\phi - \phi_0)$. We note the following dependencies across the symmetry plane:

$$\begin{aligned} Q_0(-\phi) &= Q_0(\phi) \\ Q_1(-\phi) &= Q_1(\phi) \\ \phi_g(-\phi) &= -\phi_g(\phi) \\ H(-\phi, -\phi - \phi_0) &= H(\phi, \phi + \phi_0) \end{aligned} \tag{43}$$

Accordingly, it is easy to show that the full-circle integral of Eq. 42 is equivalent to the integral over the half-circle

$$\begin{aligned} I_\phi = \int_0^\pi \Big\{ & Q_0(\phi) \left[H(\phi, \phi - \phi_0) + H(\phi, \phi + \phi_0) \right] \\ & + Q_1 \left[H(\phi, \phi - \phi_0) \cos(\phi_g(\phi) - \phi_0) + H(\phi, \phi + \phi_0) \cos(\phi_g(\phi) + \phi_0) \right] \Big\} d\phi \end{aligned} \tag{44}$$

This procedure allows the evaluation of the power spectral density by integration over the volume of the half jet.

3. Special Treatment for Axisymmetric Jets

For axisymmetric jets, the computational cost can be further reduced by confining the volume integral to an azimuthal slice of the jet. This is not a simple reduction because it needs to account for the source-observer azimuthal dependencies in A_{0000} (i.e., the cosine terms in Eq. 41a) as well as the azimuthal influence contained in $\widetilde{R}_{23}$. Having an analytical relation for $\widetilde{R}_{23}$ is very useful in this regard. The resulting expressions take different forms whether one selects $\beta_{23} = 1$ or $\beta_{23} = 2$ in Eq. 29. Accordingly, we break down the analysis for each exponent.

For $\beta_{23} = 2$ the source term H of Eq. 41(d) is expressed as

$$H = H' e^{\sigma \cos(\phi - \phi_0)} \tag{45a}$$

$$H' = \frac{\alpha^4}{16\pi R^2} \tau_* L_1 \pi L_{23}^2 \widehat{R}_1 \widehat{R}_4 \exp\Big\{ - \left(\frac{\alpha L_{23}}{2} \right)^2 \left(\sin^2 \theta_0 + \frac{1}{\mu_c^2} \right) \Big\} \tag{45b}$$

$$\sigma = \frac{(\alpha L_{23})^2 \sin\theta_0}{2\mu_c} \tag{45c}$$

Now it is assumed that the gradient-based azimuthal angle ϕ_g equals the geometric azimuthal angle ϕ. This is valid for a mean velocity profile that is monotonically decreasing with radius and is applicable to the dominant source region of the axisymmetric jets under consideration here. Then Eq. 41(a) becomes

$$S(\mathbf{x}_0, \omega) = \int_{\mathcal{V}} H' \left[Q_0 + Q_1 \cos(\phi - \phi_0) \right] e^{\sigma \cos(\phi - \phi_0)} \, d^3\mathbf{y} \tag{46}$$

Noting that H', Q_0, and Q_1 are all purely axisymmetric, the only azimuthal dependence of this integral comes from the $\cos(\phi - \phi_0)$ terms. Invoking the integral representations of the modified Bessel functions, the azimuthal component of the integration results in the terms

$$\int_{-\pi}^{\pi} e^{\sigma \cos(\phi - \phi_0)} d\phi = 2\pi I_0(\sigma) \tag{47}$$

$$\int_{-\pi}^{\pi} \cos(\phi - \phi_0) e^{\sigma \cos(\phi - \phi_0)} d\phi = 2\pi I_1(\sigma) \tag{48}$$

where I_0 and I_1 are the modified Bessel functions of the first kind and of orders zero and one, respectively. Now Eq. 46 collapses into the two-dimensional integral

$$S(\mathbf{x}_0, \omega) = 2\pi \int_0^\infty \int_0^\infty H' \big[Q_0 I_0(\sigma) + Q_1 I_1(\sigma) \big] \, y dy \, dX \tag{49}$$

While in theory the reduction to two dimensions cuts down the computational demands dramatically, the expectation of sufficiently resolved data on a given meridional section is not realistic. Computational codes

produce data in three-dimensional grids that may not purely axisymmetric (even for the treatment of axisymmetric jets) and thus cannot be readily transformed into a radial set. Interpolation on a meridional section presents numerical challenges that can introduce errors with large impact on the noise prediction, particularly in the very thin shear layers near the nozzle exit. On the other hand, restricting the integration to an azimuthal slice containing a sufficient population of elements is a very simple procedure. It is accomplished here by realizing that Eq. 49 is equivalent to

$$S(\mathbf{x}_0,\omega) \;=\; \frac{2\pi}{\Phi}\int_0^{\Phi}\int_0^{\infty}\int_0^{\infty} H'\big[Q_0 I_0(\sigma)+Q_1 I_1(\sigma)\big]\; y dy\; dX d\phi \tag{50}$$

The integral now represents a volumetric integration over an azimuthal slice of angle Φ, and can be expressed compactly as

$$S(\mathbf{x}_0,\omega) \;=\; \frac{2\pi}{\Phi}\int_{\mathcal{V}_\Phi} H'\big[Q_0 I_0(\sigma)+Q_1 I_1(\sigma)\big] d^3\mathbf{y}\;, \quad \beta_{23}=2 \tag{51}$$

where $\mathcal{V}_\Phi$ is the volume of the slice.

Now we repeat the procedure for $\beta_{23}=1$. The source term H is expressed as

$$H \;=\; H'\frac{1}{[1-\sigma\cos(\phi-\phi_0)]^{3/2}} \tag{52a}$$

$$H' \;=\; \frac{\alpha^4}{8\pi R^2}\tau_* L_1 \pi L_{23}^2 \widehat{R}_1\widehat{R}_4\left\{1+(\alpha L_{23})^2+\sin^2\theta_0+\frac{1}{\mu_c^2}\right\}^{-3/2} \tag{52b}$$

$$\sigma \;=\; \frac{2\sin\theta_0}{\mu_c\left[\frac{1}{(\alpha L_{23})^2}+\sin^2\theta_0+\frac{1}{\mu_c^2}\right]} \tag{52c}$$

On defining the special functions

$$\mathscr{D}_0(\sigma) \;=\; \frac{1}{2\pi}\int_{-\pi}^{\pi}\frac{d\phi}{[1-\sigma\cos\phi]^{3/2}} \tag{53}$$

$$\mathscr{D}_1(\sigma) \;=\; \frac{1}{2\pi}\int_{-\pi}^{\pi}\frac{\cos\phi\; d\phi}{[1-\sigma\cos\phi]^{3/2}} \tag{54}$$

and following the same arguments as for $\beta_{23}=2$, the computation of the spectral density over an azimuthal slice of volume $\mathcal{V}_\Phi$ takes the form

$$S(\mathbf{x}_0,\omega) \;=\; \frac{2\pi}{\Phi}\int_{\mathcal{V}_\Phi} H'\big[Q_0 \mathscr{D}_0(\sigma)+Q_1 \mathscr{D}_1(\sigma)\big] d^3\mathbf{y}\;, \quad \beta_{23}=1 \tag{55}$$

The special functions $\mathscr{D}_0$ and $\mathscr{D}_1$ follow similar trends as the modified Bessel functions I_0 and I_1, respectively. They are valid over $0\le\sigma<1$ and their approximations are given in Appendix B.

Through experimentation it was determined that a 5-degree azimuthal slice contained a sufficient number of elements to compute the power spectral density with excellent accuracy, within a few tenths of a decibel, as compared to integration over the entire volume. The resulting 36-fold reduction in computational time, relative to treating the entire half-jet, benefits tremendously the conjugate-gradient minimization process described in Section IV.B, which requires evaluation of the spectral density on the order of 100 times.

H. Outer Surface of Peak Stress (OSPS)

In the expression for the power spectral density of Eq. 22, the effect of the axial convection of the turbulent eddies is captured by the term

$$\widehat{R}_1\left[\alpha L_1\left(\frac{1}{M_c}-\cos\theta_0\right)\right]$$

We will call this term "radiation efficiency", realizing that this term has been used in the past under varying contexts. Here it means the efficiency with which a four-dimensional correlation volume $\tau_* L_1 \pi L_{23}^2$ radiates sound in the far field at a given frequency and for fixed correlation functions. The radiation efficiency is controlled by the convective Mach number $M_c \;=\; U_c/a_\infty$. We gain insight into the underlying physics by

considering special values of M_c. For a very low speed jet where $M_c \to 0$, the argument of $\widehat{R}_1$ becomes very large and thus $\widehat{R}_1 \to 0$. This is the limit of zero radiation efficiency. The limit $M_c = \infty$ signifies disturbances being transmitted instantaneously throughout the length of the object, like in the case of an oscillating solid cylinder. Then the radiation efficiency becomes $\widehat{R}_1(-\alpha L_1 \cos\theta_0)$ and the peak radiation occurs at $\theta_0 = 90°$. In general, the radiation efficiency peaks at $\cos\theta_0 = 1/M_c$, where the argument of R_1 is zero. For $M_c \geq 1$, this represents the well-known Mach wave emission in high-speed jets that occurs near $\theta_0 = \arccos(1/M_c)$. For $M_c < 1$ the radiation efficiency does not reach its peak value and increases monotonically towards $\theta_0 = 0$. A physical constraint in applying the above arguments is the spreading rate of the jet flow, which is around 10°. Sound emission at observer angles close to the spreading angle is bound to be influenced by flow-acoustic interactions.

The importance of the radiation efficiency term, coupled with the need to connect it to sound generated by coherent structures, make the selection of M_c one of the most critical decisions in the modeling. Here we argue that radiation efficiency is governed by the eddies of the outermost shear layer of the jet. This follows the observation that just outside the jet, in the near pressure field, the pressure distribution reflects the "footprint" of the most energetic eddies, as confirmed by several studies of single-stream jets.[36,37] For multistream jets, we pose an additional condition that these eddies be in direct contact with the ambient fluid. The noise radiated by those eddies involves a direct coupling between the turbulent motion and the sound field; this does not involve mean flow/acoustic interaction or propagation effects as long as the observer polar angle is too close to the jet spreading angle. In terms of the mean flow, and following the arguments presented in Section II.A, the action of these eddies is represented by the peak Reynolds stress of the outermost shear layer. Accordingly we define the outer surface of peak stress (OSPS) as the locus of the first peak of the Reynolds stress as one approaches the jet from the ambient towards the jet axis. Denoting the radial location of the OSPS as $y_{\text{OSPS}}(X, \phi)$, and letting $\mathbf{y} = (X, y, \phi)$ represent the location of a volume element in polar coordinates (Fig. 2), the convective Mach number of that element is defined as

$$M_c(X, y, \phi) \;=\; \frac{\overline{u}(X, y_{\text{OSPS}}(X, \phi), \phi)}{a_\infty} \tag{56}$$

This means that all the volume elements at a particular X and ϕ are assigned the same value of M_c as determined by Eq. 56.

Accurate detection of the OSPS requires very good resolution of the thin layers near the nozzle exit. The near-field region affects the mid to high frequencies and is thus of paramount importance to aircraft noise. Small errors in the location of the shear layers can lead to large errors in the determination of M_c. The detection scheme is illustrated in Fig. 9. The RANS flow field is divided into axial slices of very fine spacing near the nozzle exit and coarser spacing downstream. Each axial slice is divided into fine azimuthal segments, typically in 2.5-degree increments. Within each azimuthal segment, the data (velocity, Reynolds stress) are sorted in order of the decreasing radius y. The search process for the first (outermost) peak of the Reynolds stress starts at the radial location where the mean axial velocity is one third of the tertiary exit velocity. This is to prevent spurious detection of peaks that may occur if one starts the search further out where the velocity is very low and the data can be noisy. Denoting g_j the discrete values of the Reynolds stress, the operation

$$h_j \;=\; \max(g_j, g_{j+1})$$

is carried out as we move inward towards the jet axis. We seek the first occurrence where h_j remains invariant for J consecutive points. This indicates that the first peak of the Reynolds stress occurred at point $j - J$. The proper value of J will depend on the resolution of the RANS data (population of each axial/azimuthal segment) and needs to be determined carefully by the user. Inspection of the resulting OSPS is highly recommended to ensure the absence numerical errors. Examples of the OSPS will be shown Figs. 15 and 16.

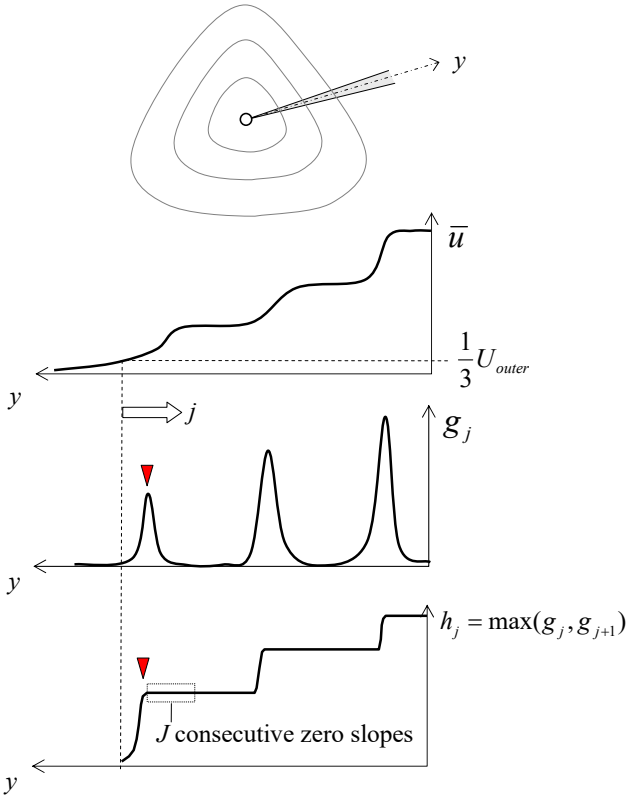

Figure 9. Detection scheme for the location of the outer peak of the Reynolds stress (red marker).

I. RANS-Based Scales

The correlation length and time scales follow the traditional definitions, based on the RANS flow field, used in past acoustic analogy models.[11] They are constructed from the turbulent kinetic energy k and the dissipation ϵ. The specific dissipation is defined as $\Omega = k/\epsilon$. The equation that follows describes the axial and transverse length scales, and the time scale.

$$\begin{aligned} L_1 &= C_1 \frac{k^{3/2}}{\epsilon} = C_1 \frac{k^{1/2}}{\Omega} \\ L_{23} &= C_{23} \frac{k^{3/2}}{\epsilon} = C_{23} \frac{k^{1/2}}{\Omega} \\ \tau_* &= C_4 \frac{k}{\epsilon} = C_4 \frac{1}{\Omega} \end{aligned} \tag{57}$$

The turbulent viscosity ν_T in Eq. 34 is obtained from the dimensional construct

$$\nu_t = c_\mu \frac{k}{\Omega} \tag{58}$$

The value $c_\mu = 0.09$ was use here.

IV. Parameterization of the Space-Time Correlation

The preceding sections described the theoretical framework for calculating the far-field spectral density as summarized in Eq. 41. The specific implementation of Eq. 41 requires selection of the parameters that control the shapes of the correlation functions R_1, R_{23}, and R_4 that comprise the space-time correlation of the Lighthill stress tensor given by Eq. 17. Here we discuss the process by which these parameters are selected.

A. Source Parameters

The prediction of the far-field spectral density is dependent on a parameter vector $\mathbf{V} = (V_1, \ldots, V_K)$ that defines the correlation functions used in formulating the space-time correlation of Eq. 17. Here the parameter vector comprises the scale coefficients C_1, C_{23}, C_4 (Eq. 57) and the exponent powers β_1, β_4 (Eq. 18). Recall that the exponent power for the cross-stream correlation was fixed at $\beta_{23} = 1$ or 2. The correlation parameters are therefore determined upon selection of β_{23}.

We denote the parameter vector

$$\mathbf{V} \ = \big[C_1, C_{23}, C_4, \beta_1, \beta_4\big] \tag{59}$$

The far-field power spectral density can then be expressed as

$$S(\mathbf{V},\ R,\ \theta_0,\ \phi_0,\ \omega\ ) \tag{60}$$

It is convenient to work with the Sound Pressure Level (SPL) spectrum, in units of decibels. The modeled SPL spectrum is

$$\mathrm{SPL}_{\mathrm{mod}}(\mathbf{V},\ R,\ \theta_0, \phi_0, \omega) \ = \ 10 \log_{10} \left[\frac{S(\mathbf{V}, R, \theta_0, \phi_0, \omega)}{S_{\mathrm{norm}}} \right] \tag{61}$$

where $S_{\mathrm{norm}} = 4 \times 10^{-10}$ Pa^2 is the commonly used normalization value. The experimental SPL spectrum is $\mathrm{SPL}_{\mathrm{exp}}(R_{\mathrm{exp}}, \theta_0, \phi_0, \omega)$ where R_{exp} is the microphone distance or the distance at which the experimental spectrum is referenced to.

B. Determination of Parameter Vector

Determination of the parameter vector is based on knowledge of the spectral density of the axisymmetric *reference* jet. Specifically, we seek a parameter vector that minimizes the difference between the modeled and experimental SPL spectra for the reference jet: $\mathrm{SPL}^{\mathrm{ref}}_{\mathrm{mod}}(\mathbf{V}, R, \theta_0, \omega)$ and $\mathrm{SPL}^{\mathrm{ref}}_{\mathrm{exp}}(R_{\mathrm{exp}}, \theta_0, \omega)$. We facilitate the optimization by normalizing the experimental and modeled spectral densities by their respective maximum values versus frequency. Equivalently, in units of decibels we subtract the maximum values. The normalization removes the effect of the distances R and R_{exp}, so the normalized spectra depend only on the parameter vector (for the modeled spectrum), the observer polar angle, and the frequency. The normalized modeled and experimental SPL spectra for the reference jet are:

$$\begin{aligned} \overline{\mathrm{SPL}}^{\mathrm{ref}}_{\mathrm{mod}}(\mathbf{V}, \theta_0, \omega) \ &= \mathrm{SPL}^{\mathrm{ref}}_{\mathrm{mod}}(\mathbf{V}, R, \theta_0, \omega) - \mathrm{SPL}^{\mathrm{ref}}_{\mathrm{mod,max}}(\mathbf{V}, R, \theta_0) \\ \overline{\mathrm{SPL}}^{\mathrm{ref}}_{\mathrm{exp}}(\theta, \omega) \ &= \mathrm{SPL}^{\mathrm{ref}}_{\mathrm{exp}}(R, \theta_0, \omega) - \mathrm{SPL}^{\mathrm{ref}}_{\mathrm{exp,max}}(R, \theta_0) \end{aligned} \tag{62}$$

This normalization removes the amplitude as a variable, so we are concerned only with matching the shape of the spectra.

We seek to minimize the difference between the modeled and experimental spectra at observer polar angle θ_0 and at a set of frequencies $\omega_n, n = 1, \ldots, N$. Accordingly, we construct the cost function

$$F(\mathbf{V}) \ = \ \sqrt{\frac{1}{N} \sum_{n=1}^{N} \left[\overline{\mathrm{SPL}}^{\mathrm{ref}}_{\mathrm{mod}}(\mathbf{V}, \theta_0, \omega_n) - \overline{\mathrm{SPL}}^{\mathrm{ref}}_{\mathrm{exp}}(\theta_0, \omega_n) \right]^2} \ + \ \sum_{k=1}^{K} P_k(V_k) \tag{63}$$

The square root represents the "error" between model and experiment in units of decibels; P_k are appropriately defined penalty functions that constrain the parameters within reasonable ranges. The parameter vector $\mathbf{V}$ is determined by minimizing the cost function. The minimization process of Eq. 63 uses the Restarted Conjugate Gradient method of Shanno and Phua[38] (ACM TOM Algorithm 500). The minimization typically used N=10 frequencies spaced at equal logarithmic intervals, covering the entire relevant part of the spectrum. The scheme converged after about 30 function calls to an error on the order of 1.0 dB and zero penalty function.

C. Application to Non-Reference Jets

Upon a reasonable match of the reference modeled and experimental spectra, the parameter vector $\mathbf{V}$ becomes determined. This parameter vector is now applied to the non-reference (typically asymmetric) jet, yielding

$\mathrm{SPL}_{\mathrm{mod}}(\mathbf{V}, R, \theta_0, \phi_0, \omega)$. Direct comparison with the SPL spectrum of the experimental non-reference jet is enabled by doing the amplitude adjustment

$$\mathrm{SPL}_{\mathrm{mod}}(\mathbf{V}, R_{\mathrm{exp}}, \theta_0, \phi_0, \omega) \;=\; \mathrm{SPL}_{\mathrm{mod}}(\mathbf{V}, R, \theta_0, \phi_0, \omega) + \mathrm{SPL}^{\mathrm{ref}}_{\mathrm{exp,max}} - \mathrm{SPL}^{\mathrm{ref}}_{\mathrm{mod,max}} \tag{64}$$

V. Application Fields

So far we have described a methodology for the acoustic prediction of symmetric and asymmetric jets, and the parameterization of the problem based the far-field sound of the baseline (symmetric) jet. Again, we are interested in predicting the noise *change* from a known baseline. In this section we describe briefly the experimental and computational data for the jets to which this methodology will be applied. An extensive review of the experimental results is available in Ref. 8.

A. Experimental

1. Experimental Setup

The experiments utilized three-stream nozzles as part of UCI's recent effort in characterizing and suppressing noise from three-stream jets representative of the exhausts of future supersonic aircraft. The nozzles comprised axisymmetric (reference) configurations as well as asymmetric configurations that involved reshaping of the outer tertiary duct. Figure 10 shows the designs of the three nozzles covered in this paper and includes the azimuthal distribution of the width of the tertiary annulus. All the nozzles shared the same exit areas. The effective (area-based) primary exit diameter was $D_{p,\mathrm{eff}} = 13.33$ mm and the area ratios were $A_s/A_p = 1.44$ and A_t/A_p=1.06. Denoting the width of the tertiary annulus W_t, and noting that $D_{p,\mathrm{eff}}$ provides a scale for the lateral extent of the strongest noise sources, we use the ratio $W_t/D_{p,\mathrm{eff}}$ to describe the relative size of the tertiary stream. The azimuthal angle ϕ is defined relative to the downward vertical direction.

Nozzle AXI03U is a coaxial design, and is used here as the reference nozzle. The tertiary annulus thickness is uniform with $W_t/D_{p,\mathrm{eff}} = 0.119$. Nozzle ECC06U features a shaped offset tertiary duct wherein the tertiary annulus becomes thicker over the azimuthal range $-110^\circ \le \phi \le 110^\circ$ and thinner outside this range. The ratio $W_t/D_{p,\mathrm{eff}}$ is constant at 0.155 over $-60^\circ \le \phi \le 60^\circ$ and thins gradually to 0.05 near the top of the nozzle. The tertiary outer wall is recessed at the top of the nozzle to prevent formation of a long thin duct. Nozzle ECC08U retains the same features of ECC06U but adds a wedge deflector at the top of the tertiary duct. The deflector dimensions are $\ell/D_{p,\mathrm{eff}}$ =1.50 and $\delta = 25^\circ$, where ℓ is the deflector length and δ is the wedge half-angle. The deflector blocks an azimuthal extent of 40° at the top of the nozzle, which allows thickening of the tertiary annulus on the underside of the nozzle while preserving the cross-sectional area. The ratio $W_t/D_{p,\mathrm{eff}}$ increases to 0.165 over $-60^\circ \le \phi \le 60^\circ$.

The tertiary exit diameters were $D_t = 31.15$ mm, 32.09 mm, and 32.19 mm for AXI03U, ECC06U, and ECC08U, respectively. The slight variation in outer diameter was due to the reshaping of the tertiary duct while maintaining constant area.

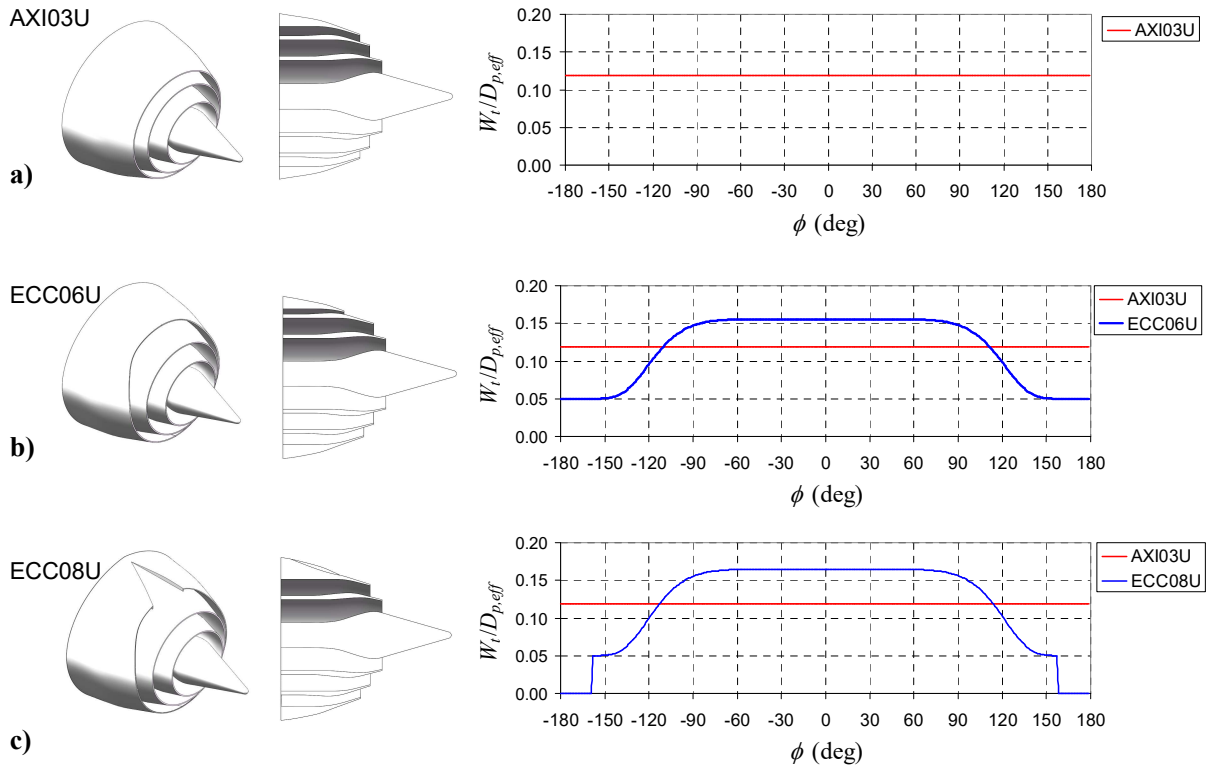

Figure 10. Three-stream nozzles. Left to right: perspective view, cross-sectional view, and azimuthal distribution of the tertiary annulus width. Azimuthal angle ϕ is defined relative to the downward vertical direction.

The nozzles were tested at cycle conditions that were representative of three-stream turbofan engines operating at takeoff power. Table 2 lists the key parameters. The Reynolds number of the primary stream was 280,000. The velocity and Mach number were matched exactly using helium-air mixture jets.[39]

Table 2 Cycle point for three-stream jets

	Primary	Secondary	Tertiary
U (m/s)	591	370	282
M	1.07	1.06	0.81
A/A_p	1.00	1.44	1.06
U/U_p	1.00	0.63	0.48

Noise measurements were conducted inside an anechoic chamber equipped with twenty four 1/8-in. condenser microphones (Bruel & Kjaer, Model 4138) with frequency response up to 120 kHz. Twelve microphones were mounted on a downward arm (azimuth angle $\phi = 0°$) and twelve were installed on a sideline arm ($\phi = 60°$). On each arm, the polar angle θ ranged approximately from 20° to 120° relative to the downstream jet axis, and the distance to the nozzle exit ranges from 0.92 m to 1.23 m. This arrangement enabled simultaneous measurement of the downward and sideline noise at all the polar angles of interest. The microphones were connected, in groups of four, to six conditioning amplifiers (Bruel & Kjaer, Model 2690-A-0S4). The 24 outputs of the amplifiers were sampled simultaneously, at 250 kHz per channel, by three 8-channel multi-function data acquisition boards (National Instruments PCI-6143) installed in a Dell Precision T7400 computer with a Xeon quad-core processor. National Instruments LabView software is used to acquire the signals. The temperature and humidity inside the anechoic chamber are recorded to enable computation of the atmospheric absorption. The microphone signals were conditioned with a high-pass filter set at 300 Hz. Narrowband spectra were computed using a 4096-point Fast Fourier Transform, yielding a frequency resolution of 61 Hz. The spectra were corrected for microphone actuator response, microphone

free field response and atmospheric absorption, thus resulting in lossless spectra. For the typical testing conditions of this experiment, and for the farthest microphone location, the absorption correction was 4.5 dB at 120 kHz.

2. *Acoustic Results*

Figure 11 plots SPL spectra in the downward direction ($\phi = 0°$) for jets AXI03U, ECC06U, and ECC08U. ECC06U offers reductions on the order of 10 dB at polar angles near the angle of peak emission and in the medium to high frequency range. Addition of the wedge deflector in nozzle ECC08U increases these reductions to $\sim$ 15 dB. Noise emission in the broadside direction ($\theta \approx 90°$) is not significantly changed or shows a slight increase.

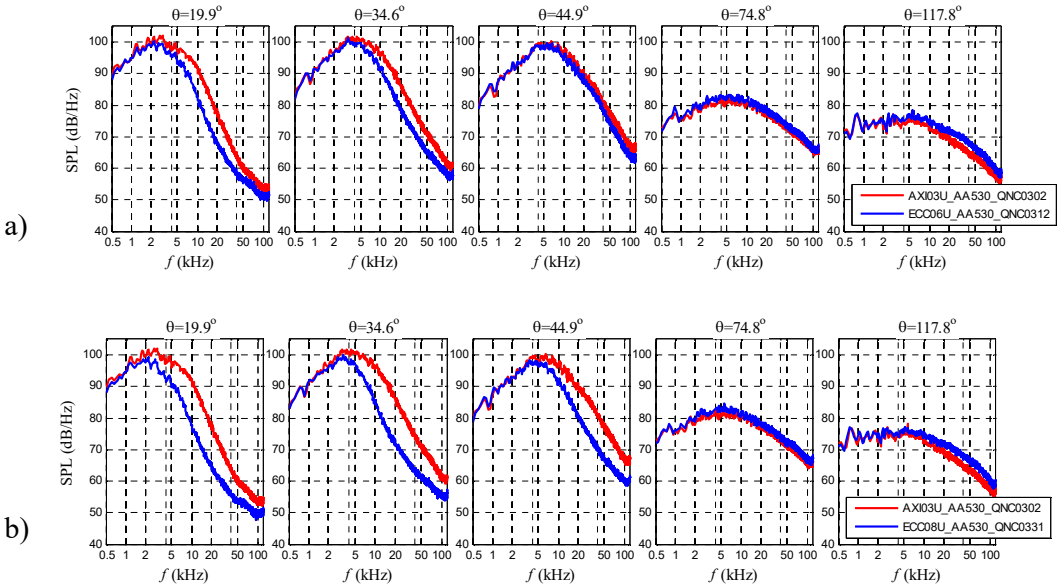

Figure 11. Narrowband far-field spectra for jets a) ECC06U and b) ECC08U with comparison to reference AXI03U jet (red) for various polar angles θ. Azimuthal direction $\phi = 0°$ (downward).

B. Computational

1. *Code*

The computational fluid dynamics code used here is known as PARCAE[40] and solves the unsteady three dimensional Navier-Stokes equations on structured multiblock grids using a cell-centered finite-volume method. Information exchange for flow computation on multiblock grids using multiple CPUs is implemented through the MPI (Message Passing Interface) protocol. In its time-averaged implementation, the code solves the RANS equations using the Jameson-Schmidt-Turkel dissipation scheme[41] and the Shear Stress Transport (SST) turbulence model of Menter.[42] The SST model combines the advantages of the $k - \Omega$ and $k - \epsilon$ turbulence models for both wall-bounded and free-stream flows.

The governing equations were solved explicitly in a coupled manner using five-stage Runge-Kutta scheme toward steady state with local time stepping, residual smoothing, and multigrid techniques for convergence acceleration. Only the steady-state solution was considered because we are interested in the time-averaged features of the flow. The computation encompassed both the internal nozzle flow as well as the external plume. The computational domain extended to 38 tertiary nozzle diameters D_t downstream and $8D_t$ radially. As all the configurations were symmetric about the meridian plane, only one-half of the domain was modeled to save computational cost. The typical grid contained 8 million points. The grid was divided into multiblocks to implement parallelization on multiprocesor computers to reduce the convergence time. For the primary, secondary, and tertiary duct flows, uniform total pressure was specified at the inlet surface corresponding to the perfectly expanded exit Mach number. For the ambient region surrounding the nozzle

flow, a characteristic boundary condition was defined, and the downstream static pressure was set equal to the ambient pressure. Adiabatic no-slip boundary condition was specified on all nozzle walls.

The code has been used in past research on dual-stream symmmetric and asymmetric jets, and its predictions have been validated against mean velocity measurements.[43] In addition to providing information on the plume flow field, the code also predicts the aerodynamic performance of the nozzles. Here the code was applied at the conditions shown in Table 1 and the experimental Reynolds numbers.

The optimization scheme of this study would have been prohibitively expensive using the full computational grids of around 8 million points. Post processing of the RANS data to reduce the computational requirements and perform the steps necessary for the modeling (e.g., centroid location, OSPS detection, etc.) is an essential task that requires the utmost care. Details of the post processing are covered in Appendix A.

2. *Relevant Statistics*

The presentation of the RANS solution starts with contour maps of the mean axial velocity on the symmetry $(X-Y)$ plane, shown in Fig. 12. $x=0$ signifies the location of the plug tip. For the axisymmetric jet AXI03U, the high-speed region extends to about seven tertiary diameters. The asymmetric delivery of the tertiary stream shortens moderately the high speed region on $x/D_t \approx 6.5$ for jet ECC06U and $x/D_t \approx 6.0$ for jet ECC08U. For the asymmetric jets, the thickening of the low speed flow on the underside of the jet is evident. Some distortion of the high-speed region is also noticeable. The plug wake is evident for all the jets.

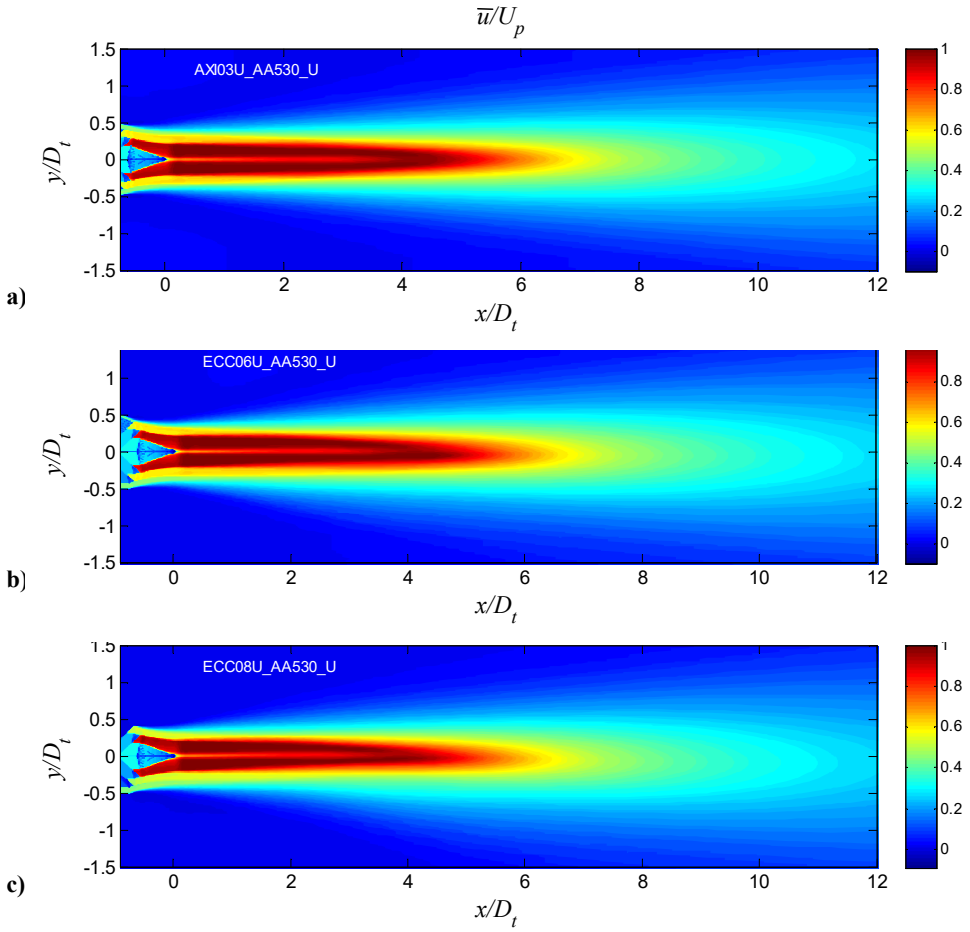

Figure 12. Distribution of normalized mean axial velocity $\overline{u}/U_p$ on the symmetry plane of jets: a) AXI03U; b) ECC06U; and c) ECC08U.

Figure 13 plots the corresponding distributions of the normalized turbulent kinetic energy k/U_p^2. For jet AXI03U, in the vicinity of the nozzle exit we can distinguish clearly the outer shear layer (between the

tertiary stream and the ambient) and the weaker inner shear layer (between the primary and secondary streams). The middle shear layer (between the secondary and tertiary streams) is not apparent. We gain an understanding of the relative strengths of the shear layers by considering that the turbulent kinetic energy (or any component of the Reynolds stress) scales approximately as $(\Delta U)^2$, where ΔU is the velocity difference across a particular shear layer. It is insightful to assess the strengths in terms of the dimensionless ratio

$$r_k \;=\; \frac{(\Delta U)^2}{(U_{max} - U_\infty)^2}$$

where the denominator signifies the largest possible strength, with U_{max} the maximum fully-expanded velocity (in this case, the primary exit velocity) and U_∞ the ambient velocity (in this case, zero). From the values of Table 2 we have $r_k = 0.139$, 0.022, and 0.228 for the inner, middle, and outer shear layer, respectively. This dimensional argument helps explain the dominance of the outer shear layer and the near-invisibility of the middle shear layer. At approximately $x/D_t = 2.5$ the secondary and tertiary streams are completely merged with primary shear layer. Now the primary eddies are in direct contact with the ambient, resulting in a rapid increase in the turbulent kinetic energy which reaches its maximum value near $x/D_t = 5.5$. Here the ratio r_k is close to unity. The location of peak turbulent kinetic energy is very close to the end of the primary potential core, as delineated by the cone-like region of very low turbulent intensity. Further downstream, the turbulent kinetic energy declines as the jet mean velocity drops. It is notable that at large downstream distances the profile for the turbulent kinetic energy becomes Gaussian-like.

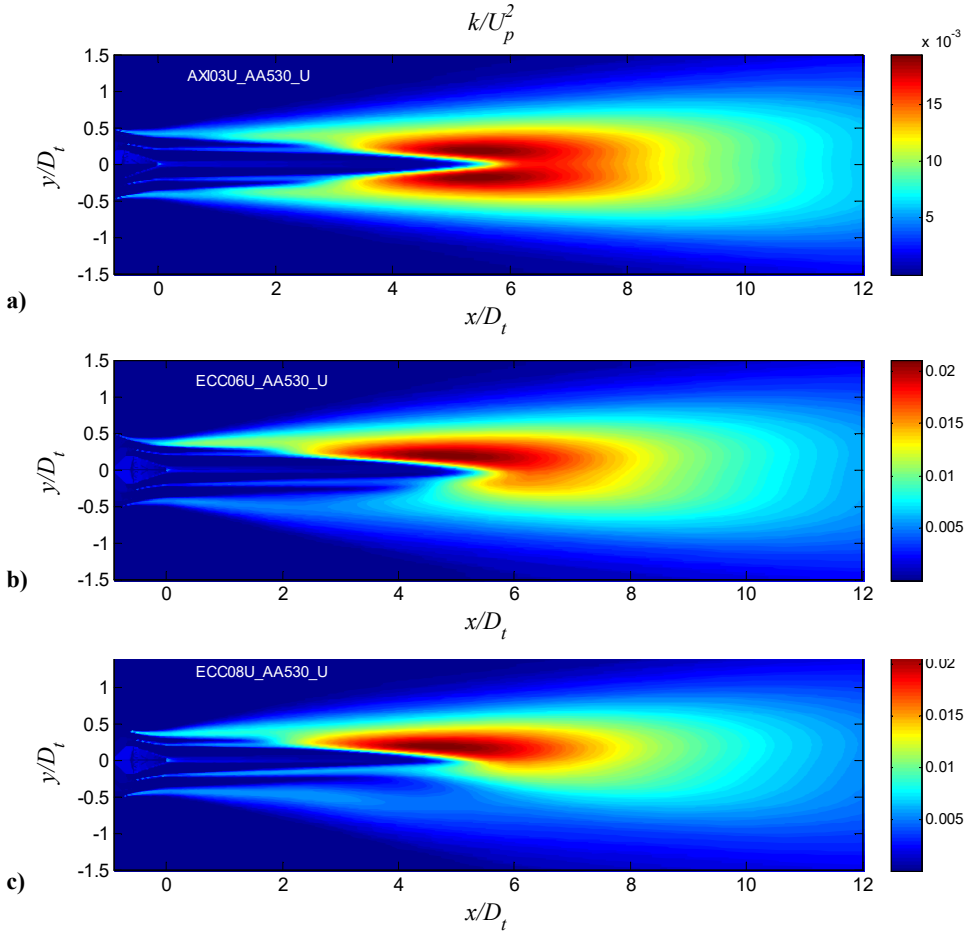

Figure 13. Distribution of normalized turbulent kinetic energy k/U_p^2 on the symmetry plane of jets: a) AXI03U; b) ECC06U; and c) ECC08U.

For the asymmetric jets ECC06U and ECC08U the secondary and tertiary streams extend much longer on the underside of the jet, reaching $x/D_t = 4$ for ECC06U and $x/D_t = 5$ for ECC08U. Their elongation

prevents the contact of the primary eddies with the ambient until past the end of the primary core. As a result, the turbulent kinetic energy on the underside of the jet is significantly reduced; this effect is most pronounced for jet ECC08U. The primary potential core is moderately reduced to $x/D_t = 5.2$ for ECC06U and $x/D_t = 4.8$ for ECC08U. All these trends bode well for noise reduciton in the downward reduction. However, looking at the distributions of Figs. 13b and 13c one has difficulty drawing a line distinguishing unambiguously the upper and lower sides of the jet.

We now turn our attention to the distribution of the normalized "Reynolds stress" g/U_p^2, depicted in Fig. 14. The distribution of g near the nozzle exit is very similar to that of k, so the same arguments apply there. However, further downstream we note a significant difference between the g and k fields. The g field has a clear minimum in the interior of the jet, which is practically zero once the wake region dissipates. The location of the minimum coincides with the jet centroid defined by Eq. 13. Downstream of the end of the potential core, the distribution of g has two lobes representing the turbulence production near the edge of the jet. Compare with the Gaussian-like profile for k in Fig. 13. We can clearly delineate the upper and lower sides of the jet, as demarkated by the location of the minimum g. The lower side experiences dramatic reductions in g, particularly in jet ECC08U. These results reinforce the view discussed in Section II.A that the Reynolds stress is the appropriate statistical quantity to represent the action of the turbulent eddies.

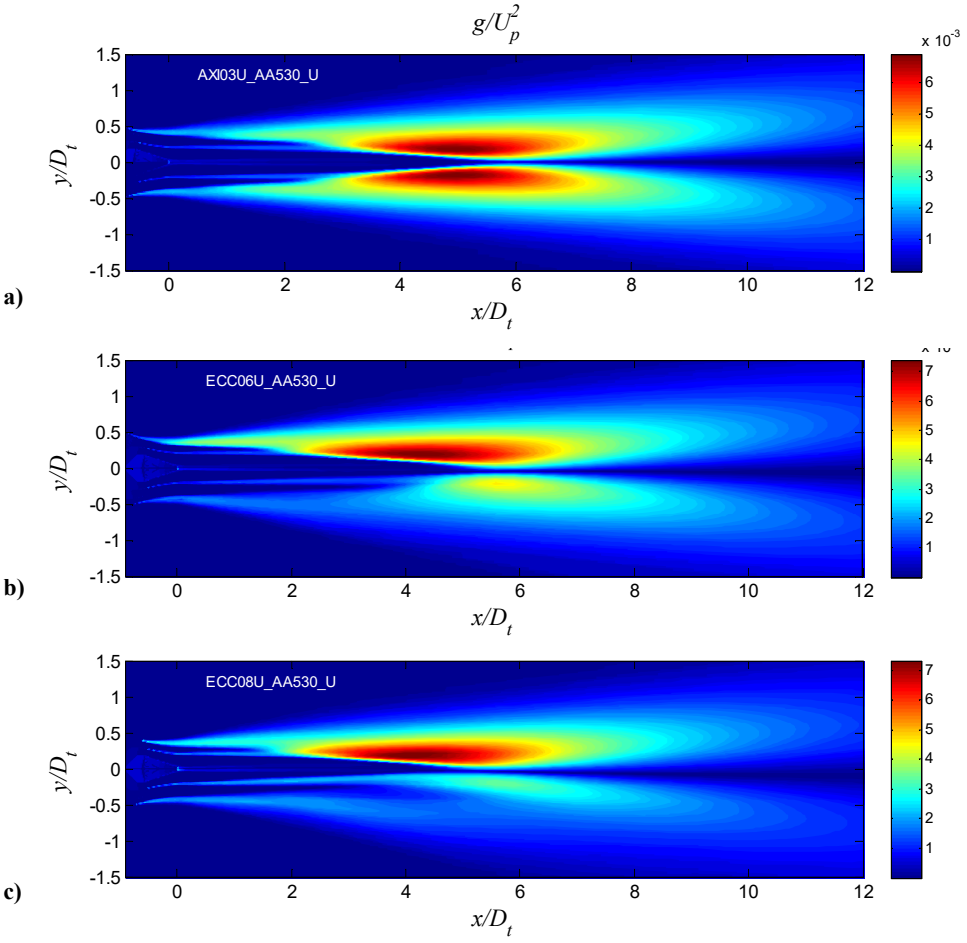

Figure 14. Distribution of normalized Reynolds stress g/U_p^2 on the symmetry plane of jets: a) AXI03U; b) ECC06U; and c) ECC08U.

3. OSPS

We now examine the geometry of the outer surface of peak stress. Figure 15 plots the location of the OSPS on the symmetry plane of jets AXI03U and ECC08U. The plots of the OSPS are overlaid on contour maps of the Reynolds stress g. For the axisymmetric jet, the OSPS experiences a sudden convergence where the

outer streams become totally mixed with the primary shear later, near $x/D_t = 2.5$. This is followed by a gradual convergence near the end of the primary potential, downstream of which the OSPS diverges slowly. For the asymmetric jet, the OSPS on the top side of the jet is similar to that for the axisymmetric jet. On the bottom side, the OSPS slightly diverges in the initial region of the jet, then suddenly shifts inward near $x/D_t = 5$, the location where the outer streams are totally mixed with the primary stream. For the first five diameters or so the OSPS on the bottom side is in a low velocity region of the jet, meaning that the convective Mach number there is low subsonic. This has a large impact on the prediction of noise emission from this region. Figure 15 also depicts the location of the centroid, which is seen to coincide with the locus of minimum Reynolds stress.

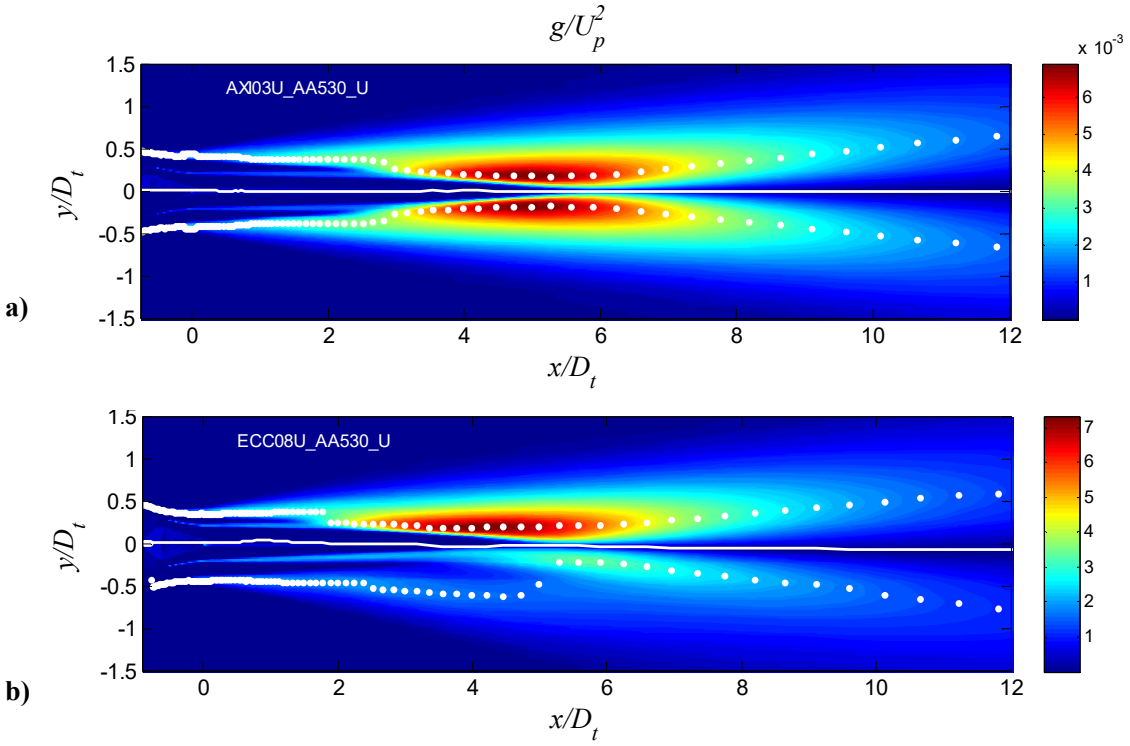

Figure 15. Location of the outer surface of peak stress (OSPS) on the symmetry plane of jets a) AXI03U and b) ECC08U. Contour map shows the Reynolds stress field g/U_p^2. White dots indicate the location of the outermost peak of g. Solid white line is the jet centroid as defined in Eq. 13.

We gain further insight by examining three-dimensional views of the OSPS, plotted in Fig. 16. The distribution of the convective Mach number M_c is shown as contour levels on the surfaces. The views cover the axial range $-0.5 \leq x/D_t \leq 10$. For jet AXI03U, the transition of the OSPS from the tertiary to the secondary to the primary shear layer is evident. The convective Mach number reaches the peak value of 1.20 shortly downstream of the transition to the primary shear layer. For jets ECC06U and ECC08U we observe a progressively stronger reshaping of the OSPS, starting at the lateral sides and progressing to the lower side. For jet ECC08U, on the underside of the OSPS, the convective Mach number is as low as 0.35. This corresponds to the order of 10-fold reduction in radiation efficiency in that region. On the upper half of the jet, the shape of the OSPS and the M_c distributions are similar to those of the axisymmetric case.

It is also instructive to examine the distribution of M_c versus axial and azimuthal directions, as is done in Fig. 17. The largest reduction in M_c occurs in the downward direction $\phi = 0$. There the peak value of M_c reduces from 1.2 for AXI03U to 1.0 for ECC06U to 0.8 for ECC08U. It is also noted that the distribution of the peak becomes confined to only about one diameter for ECC08U, versus three diameters for AXI03U. For ECC08U, the low-M_c region persists up to about $\phi = 50°$, after which the distribution becomes similar to that of the axisymmetric jet. The significant improvement in suppression of convective Mach number in jet ECC08U, versus jet ECC06U, came from a rather subtle reshaping of the tertiary duct, as illustrated in Fig. 10. This underscores the sensitivity of the offset-stream method to the fine details of the duct reshaping.

The information presented in Figs. 16 and 17 comprises the most important feedback one can obtain from the RANS solution before proceeding to the acoustic analogy step. Examinations of the OSPS and the associated M_c distribution provide strong clues whether a particular nozzle arrangement will produce a quiet jet and in what azimuthal directions. In the particular examples shown here, one can expect jet ECC08U to bring significant noise benefits in the downward direction but perhaps not as much in the sideline direction (near $\phi = 60°$).

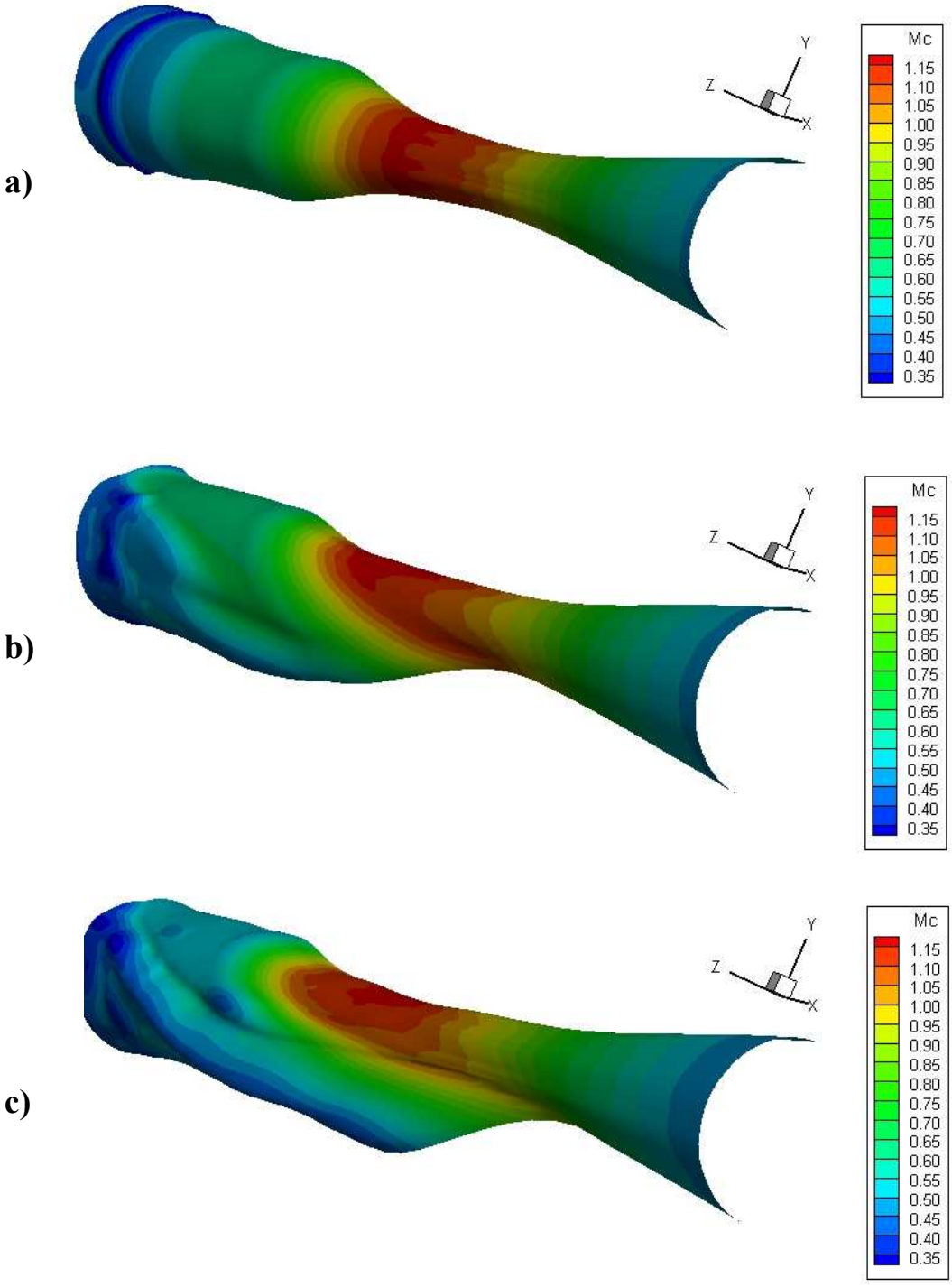

Figure 16. Outer surface of peak stress (OSPS) for jets a) AXI03U, b) ECC06U, and c) ECC08U. Contour levels show distribution of M_c on the OSPS.

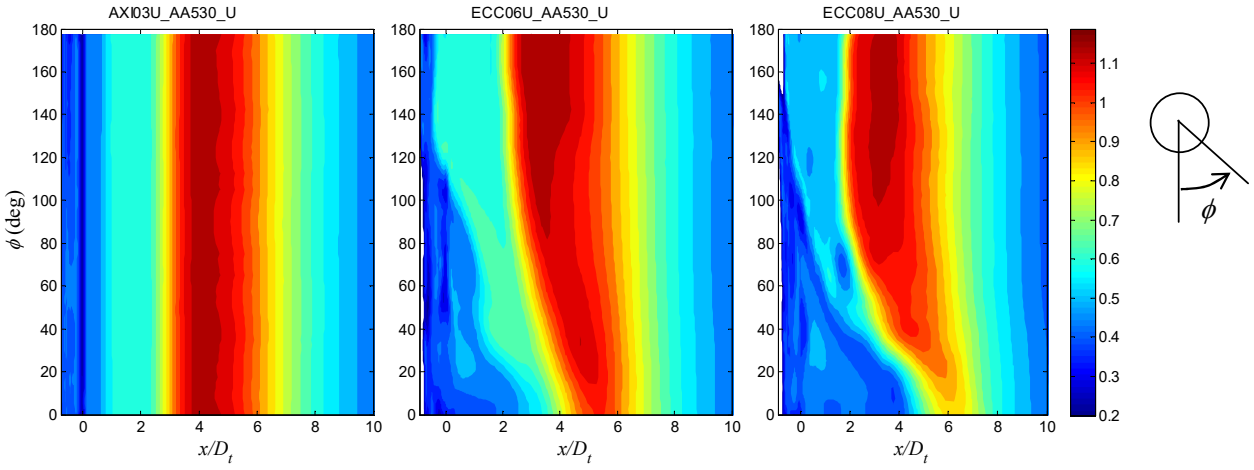

Figure 17. Axial-azimuthal distribution of convective Mach number M_c for jets AXI03U (left), ECC06U (middle), and ECC08U (right).

VI. Results

This study has introduced several new elements in the acoustic analogy modeling of peak noise from high-speed turbulent jets including: a broader class of functions for expressing the space-time correlation; definition of convective Mach number based on the locus of peak Reynolds stress; and azimuthal directivity formulation based on a transverse space-time correlation. This section presents representative results of this modeling effort, with application to the jets reviewed in Section V. All the results shown are in the direction of peak emission $\theta_0 = 35°$. The transverse convective Mach number was selected to be $\mu_c = 1.52$.

In the discussion of the sound pressure level spectra, the frequency will be presented in the non-dimensional (Strouhal number) form

$$S_r = \frac{fD_t}{U_p} = \frac{\omega D_t}{2\pi U_p} \tag{65}$$

This compound version of the Strouhal number tries account for the overall diameter of the jet, which is largely controlled by diameter of the tertiary duct, and the maximum velocity of the flow.

Application of the conjugate gradient method outlined in Section IV.B, with $\beta_{23} = 2$, resulted in the following parameter vector for the reference jet AXI03U:

$$\begin{aligned} C_1 &= 5.11 \\ C_{23} &= 3.89 \\ C_4 &= 0.39 \\ \beta_1 &= 1.73 \\ \beta_4 &= 1.96 \end{aligned} \tag{66}$$

Figure 18 plots the experimental and modeled spectra for jets AXI03U (reference) and ECC06U at observer azimuthal angles $\phi_0 = 0°$ (downward) and $\phi_0 = 60°$ (sideline). First we note the excellent match for the reference spectra. In the downward direction, the model predicts the noise reduction accurately up to $S_r \approx 2$, with a small over-predicton at higher Strouhal numbers. In the sideline direction, the model indicates marginal noise reduction which is in line with the experiment.

Similar information is displayed for jet ECC08U in Fig. 19. The acoustics of this jet were surveyed at a larger set of azimuthal angles, ranging from $\phi_0 = 0°$ (downward) to $\phi_0 = 180°$ (upward). The larger downward noise reduction of jet ECC08U is captured well by the model, as are the trends with increasing azimuthal angle. For $\phi_0 > 60°$, the experiment indicates moderate noise increase, which is generally reproduced by the model.

The results of Fig. 19 can be summarized in the form of the change in overall sound pressure level (OASPL) versus azimuthal angle. The OASPL was computed by integrating versus frequency the modeled

and experimental spectra. It is presented in two forms, the unweighted version and the A-weighted version. The A-weighted version accounts for the human perception of sound and is based on a scale factor of 40. For the A-weighted version, the SPL spectra were scale up and "corrected" with the A-weight, using the formula in the ANSI S1.43 standard.[44] The plots of ΔOASPL are shown in Fig. 20. It is seen that the model captures the azimuthal variation of the noise. For the unweighted OASPL, the model over-predicts the reduction by about 2 dB in the downward direction. The agreement is much better for the A-weighted OASPL because it is strongly influenced by the mid frequencies where the model generally performs well.

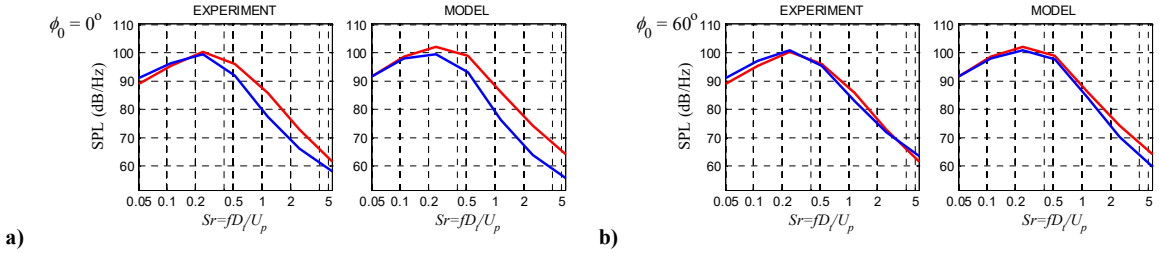

Figure 18. Experimental and modeled spectra for jets AXI03U (red) and ECC06U (blue) at polar angle $\theta_0 = 35°$. a)$\phi_0 = 0°$; b)$\phi_0 = 60°$.

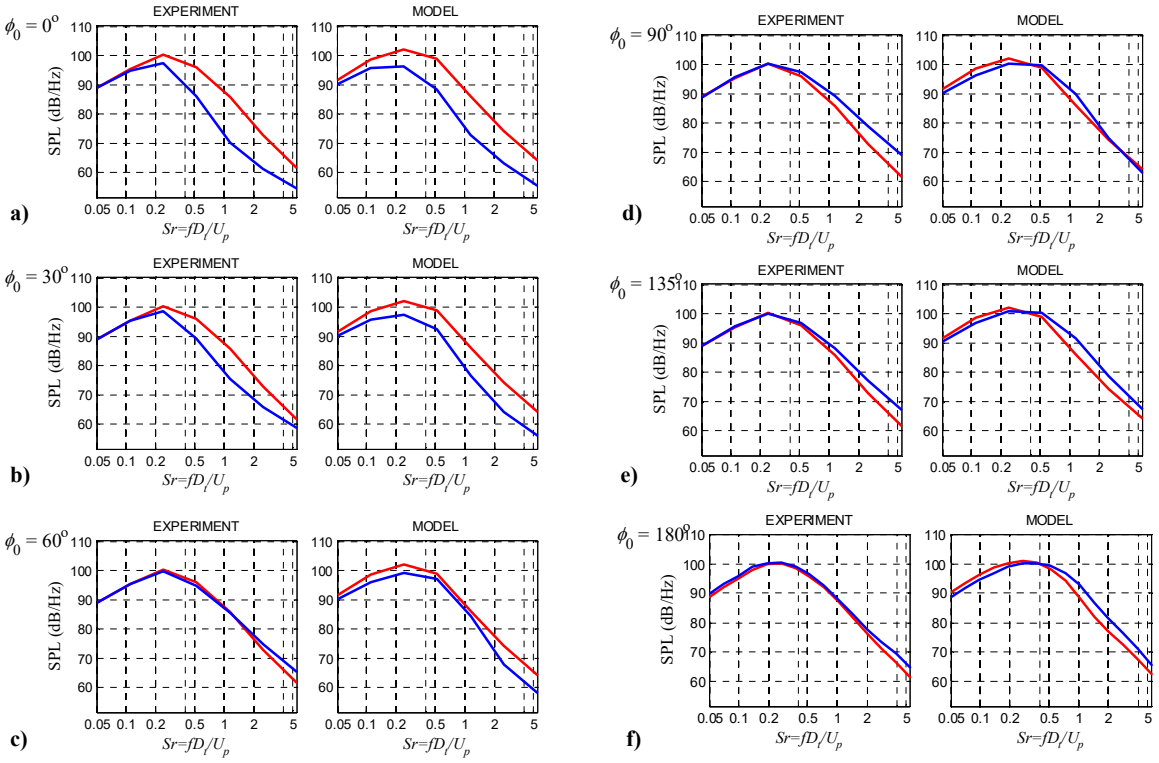

Figure 19. Experimental and modeled spectra for jets AXI03U (red) and ECC08U (blue) at polar angle $\theta_0 = 35°$. a)$\phi_0 = 0°$; b)$\phi_0 = 30°$; c)$\phi_0 = 60°$; d)$\phi_0 = 90°$; e)$\phi_0 = 135°$; f)$\phi_0 = 180°$.

VII. Conclusions

This study was motivated by the need for an engineering tool to predict the noise changes in complex, multistream jets when the geometry of the nozzle is altered. Particular emphasis is placed on asymmetric arrangements that cause directional noise suppression. A RANS-based acoustic analogy framework was developed that addresses the noise in the polar direction of peak emission and uses the Reynolds stress as

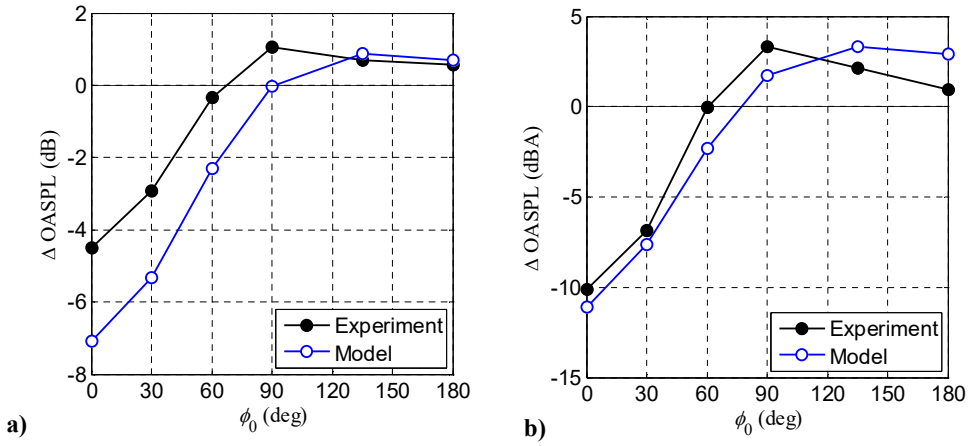

Figure 20. Experimental and modeled changes in the overall sound pressure level versus observer azimuthal angle, in the direction of peak emission, for jet ECC08U with jet AXI03U as reference. a) No weighting; b) A-weighting using scale factor of 50.

a time-averaged representation of the action of the coherent turbulent structures. The framework preserves the simplicity of the original acoustic analogy formulation by Lighthill, using the free-space Green's function, while accounting for azimuthal effects via special forms for the space-time correlation combined with source-observer relations based on the Reynolds stress distribution in the jet plume. Below we summarize the main features of this framework and comment on its application.

A central premise in the model is that the sound emission is strongly influenced by the dynamics of the *outer* shear layer of the multistream jet. In a time-averaged sense, we place attention on the outermost peak of the Reynolds stress, resulting in the definition of the outer surface of peak Reynolds stress (OSPS). The mean axial velocity on this surface is thought to best represent the convective velocity of the eddies primarily responsible for peak noise emission. The axial convective Mach number, which controls the radiation efficiency, is defined accordingly. The resulting OSPS surface and convective Mach number distribution on this surfaces provide strong clues as to the noise reduction potential of a particular nozzle configuration.

To model the azimuthal effects, it was necessary to utilize a polar coordinate system centered around a properly re-defined jet axis (Fig. 2). The new jet axis passes through the minimum value of the magnitude of the Reynolds stress inside the jet plume, and is computed practically as the centroid of the high-speed region of the jet. The use of the polar coordinate system imposes certain constraints on the types of correlations that can be used on the cross-stream plane. Source separations cannot be described in separable coordinates, necessitating the use of a mixed radial-azimuthal correlation. The usual four-dimensional Fourier transform, that gives the wavenumber-frequency spectrum in conventional formulations, is no longer possible or physical. Instead, a Hankel transform on the cross-stream plane is used in conjunction with Fourier transforms in the timewise and axial directions.

Modeling of the space-time correlation of the Lighthill stress tensor is the most critical step in any acoustic analogy effort. Here the space-time correlation is defined in a fixed frame of reference. Its axial-timewise formulation is designed to reproduce qualitatively the key features of the axial space-time correlation measured by a large number of past works, and uses the aforementioned definition of axial convective velocity. The cross-stream correlation is based on the projected distance between two source elements, a formulation that helps ensure that the modeled power spectral density is real and non-negative. An important feature is the inclusion of a transverse space-time correlation and associated transverse convective velocity. In conjunction with the Hankel transform mentioned previously, the transverse propagation induces an azimuthal directivity in the far-field spectral density. The axial and timewise correlation functions are modeled as stretched exponentials, enabling a flexibility that is very significant for calibrating the model. The cross-stream correlation is limited to exponential or Gaussian forms for numerical efficiency.

The acoustic analogy model is calibrated based on knowledge of the spectral density of a reference (axisymmetric) jet. In the present study, a five-element parameter vector controls the characteristic scales and shape coefficients of the correlation functions. The vector is determined via conjugate-gradient minimization of a cost function comprising the difference between the modeled and experimental spectra of the reference

jet as well as penalty functions that constrain the parameters. This parameter vector is then applied to the non-reference jets.

We presented results for three triple-stream jets, one axisymmetric (reference) and two asymmetric. All three jets shared the same set point. The asymmetric jets featured coaxial primary and secondary ducts, and eccentric tertiary ducts. There is an excellent match between the experimental and modeled reference jets. The model captures the azimuthal noise trends of the asymmetric jets, and reproduces reasonably well the measured noise reduction. The azimuthal variation of the A-weighted OASPL, in particular, is reproduced with an accuracy of about 1 dB.

In terms of the speed of the prediction, once a RANS solution is available the spectral density of the jet can be computed in a time frame of the order of one hour on a regular desktop computer. This includes the post-processing of the RANS data (Appendix A), conjugate-gradient determination of the parameter vector for the reference jet, and computation of the spectral density of the non-reference jet. The efficiencies discussed in Section III.G are critical for achieving rapid turnaround times. The post-processed RANS data require careful scrutiny before the acoustic analogy step. Of critical importance is the shape of the OSPS surface (Fig. 16), whose detection can be tricky. Small errors in the location of the surface can lead to large errors in the convective Mach number. Future efforts will focus on increasing the robustness of the detection scheme for the OSPS. Additional areas of attention include refinements in the modeling of the tranverse convective Mach number and a rigorous formulation of constraints to be placed on the parameter vector. In the longer term, it would be desirable to extend the model to all polar angles of relevance to aircraft noise. As discussed in Section II, the propagation aspects become less straightforward, necessitating a mix of physical insight and empiricism if the simplicity of the current framework is to be retained.

Appendix A: Post Processing of the RANS Solution

Post processing of the RANS solution comprises procedures that are critical for the proper application of the acoustic analogy model described in this paper. The procedures reflect the fundamental requirements for treating jets with azimuthally varying flow, discussed throughout the main section of the paper. Figure A1 illustrates the nature of these procedures. The first step is definition of an axial vector $X_i, i = 1, \ldots N_X$ with sufficient resolution to capture the details of the flow, particularly in the vicinity of the nozzle exit. For a regular grid the vector can coincide with the computational $X-$vector. For an irregular grid or multigrid, the vector is prescribed by the user and the computational elements are classified according to their axial location. The set of elements within a given axial sector is defined as

$$E_i \;=\; \{X \in [X_i, X_{i+1}]\}$$

The centroid of the high-speed region is computed for each X_i by applying Eq. 13 to the corresponding set E_i. The resulting centroid coordinate Y_{c_i} is then subtracted from the Y coordinates of all the elements in E_i such that $Y = 0$ becomes their centroid location.

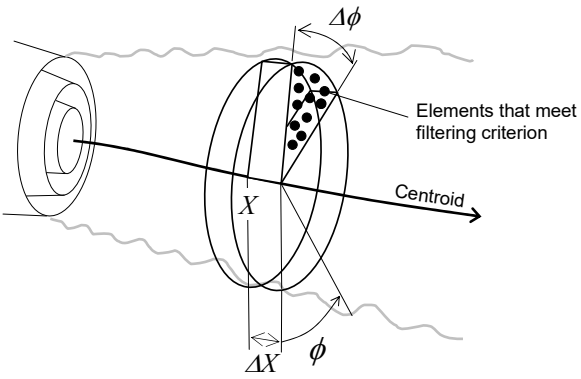

Figure A1. Post-processing of the RANS data: division of domain into axial and azimuthal sectors.

In this new coordinate system, the azimuthal angle ϕ of each element in E_i is computed. Thereafter, each axial sector is subdivided into azimuthal sectors defined by the vector $\phi_j, j = 1, \ldots, N_\phi$. The angle of each

azimuthal sector should be fine enough to resolve the azimuthal variations of the flow and large enough to contain a sufficient number of elements to determine accurately the statistics described below. In this study, a uniform azimuthal increment of 5 degrees was found to satisfy both considerations. Now the elements are categorized according to their axial and azimuthal sectors:

$$E_{ij} \;=\; \{X \in [X_i, X_{i+1}]\} \cap \{\phi \in [\phi_j, \phi_{j+1}]\}$$

The next step is identification of the location of the outer peak of the Reynolds stress within each set E_{ij} according to Section III.H.

The computational domain contains elements that make very small contribution to the noise emission. To reduce the computational cost, it is important to exclude those elements. The filtering criterion is based on the magnitude of the integrand in the relation for the spectral density, Eq. 41. Realizing that the correlation transforms $\widehat{R}_1$, $\widetilde{R}_{23}$ and $\widehat{R}_4$ govern the shape, rather than the magnitude, of the spectrum, we focus on the group

$$A_{0000}\ \tau_* L_1 \pi L_{23}^2$$

As shown in Eq. 40, the amplitude A_{0000} contains a term that is proportional to the turbulent kinetic energy k and a term that is proportional to the dominant component of the Reynolds stress g. The latter term tends to be the weaker one. It is nevertheless important to resolve it accurately, so we set the magnitude of A_{0000} at $(\overline{\rho}\ \overline{u})^2 g$. Combining with the dimensional constructs for the correlation scales presented in Eq. 57, we have

$$A_{0000}\ \tau_* L_1 \pi L_{23}^2 \quad\sim\quad (\overline{\rho}\ \overline{u})^2 g \frac{k^{3/2}}{\Omega^4}$$

When we examine the entire integral of Eq. 22, the specific dissipation Ω appears in the form $(\omega/\Omega)^4$, thus contributes to the shape, rather than the amplitude, of the spectrum, much like the correlation transforms. We thus omit Ω from consideration and define the "noise source strength", for the purpose of filtering, as

$$\text{strength} \;=\; (\overline{\rho}\ \overline{u})^2\ g\ k^{3/2} \tag{A1}$$

Let $\mathcal{S}_{ij}$ denote the *maximum* value of the noise source strength in the set E_{ij}. For each axial sector i, the azimuthal distribution of $\mathcal{S}_{ij}$ has a minimum value $\mathcal{Q}_i$. Identification of the minimum is important for asymmetric jets where there can be very large azimuthal variations of the noise source strength; filtering should depend on the minimum value of $\mathcal{S}_{ij}$ so that the spectral density on the quiet side of the jet is well resolved. Accordingly, $\mathcal{Q}_i$ is used as the criterion for filtering the RANS data. It has a global maximum $\mathcal{Q}_{\max}$ at $X = X_{\mathcal{Q}_{\max}}$. The passing criterion for an element in the set E_i is

$$\begin{aligned} s &> B_1 \mathcal{Q}_i, \qquad & X &\le C X_{\mathcal{Q}_{\max}} \\ s &> B_2 \mathcal{Q}_{\max}, \qquad & X &> C X_{\mathcal{Q}_{\max}} \end{aligned} \tag{A2}$$

where B_1, B_2 and C are constants. The rationale of Eq. A2 is that elements in the near field of the jet are filtered based on the local value of $\mathcal{Q}$, while elements in the far field of the jet are filtered based on the global maximum of $\mathcal{Q}$. The latter criterion accounts for the fast decay of the noise source strength with downstream distance past the end of the primary potential core. Typically $X_{\mathcal{Q}_{\max}}$ marks the end of the high-speed region of the jet, where the maximum local mean velocity drops below 90% of the primary exit velocity. In this study, the values $B_1 = 0.01$, $B_2 = 0.01$ and $C = 1.5$ enabled significant filtering while preserving the accuracy of the spectral density. The computational elements were reduced by about 60% while the spectral density was within 0.01 dB of the spectral density computed using the full grid.

Appendix B: Special Functions

We present the approximations of the special functions

$$\mathscr{D}_0(x) \;=\; \frac{1}{2\pi}\int_{-\pi}^{\pi} \frac{d\phi}{[1 - x\cos\phi]^{3/2}} \tag{B1}$$

$$\mathscr{D}_1(x) \;=\; \frac{1}{2\pi}\int_{-\pi}^{\pi} \frac{\cos\phi\ d\phi}{[1 - x\cos\phi]^{3/2}} \tag{B2}$$

that arise in the evaluation of the axisymmetric spectral density for $\beta_{23} = 1$. The following formulae provide fits with R^2 values of 0.99995 and are valid in the range $0 \leq x < 1$.

$$\begin{aligned} (1-x)\mathscr{D}_0(x) &= 1 + C_1 x + C_2 x^2 + C_3 x^3 \\ C_1 &= -0.9689865 \\ C_2 &= 0.6954263 \\ C_3 &= -0.2750582 \end{aligned} \tag{B3}$$

$$\begin{aligned} (1-x)\mathscr{D}_1(x) &= C_1 x + C_2 x^2 + C_3 x^3 \\ C_1 &= 0.7361897 \\ C_2 &= -0.6002907 \\ C_3 &= 0.3054138 \end{aligned} \tag{B4}$$

Acknowledgments

This work was supported by NASA Cooperative Agreement NNX14AR98A, monitored Dr. James Bridges. The author thanks Dr. Vincent Phong and Dr. Juntao Xiong for their contributions in the experiments and computations, respectively.

References

[1]Brown, C., Bridges, J., and Henderson, B., "Offset-Stream Technology Test - Summary of Results," AIAA 2007-3664, January 2007.

[2]Henderon, B., "Fifty Years of Fluidic Injection for Jet Noise Reduction," *International Journal of Aeroacoustics*, Vol. 9, No. 1 & 2, 2010, pp. 91–122.

[3]Papamoschou, D. and Debiasi, M., "Directional Suppression of Noise from a High-Speed Jet," *AIAA Journal*, Vol. 39, No. 3, 2001, pp. 380–387.

[4]Papamoschou, D., "New Method for Jet Noise Reduction in Turbofan Engines," *AIAA Journal*, Vol. 42, No. 11, 2004, pp. 2245–2253.

[5]Henderson, B., "Aeroacoustics of Three-Stream Jets," AIAA 2012-2159, June 2012.

[6]Papamoschou, D., Xiong, J., and Liu, F., "Reduction of Radiation Efficiency in High-Speed Jets," AIAA 2014-2619, June 2014.

[7]Henderson, B., Leib, S., and Wernet, M., "Measurements and Predictions of the Noise from Three-Stream Jets," AIAA 2015-3120, Jan. 2015.

[8]Papamoschou, D., Phong, V., Xiong, J., and Liu, F., "Quiet Nozzle Concepts for Three-Stream Jets," AIAA 2016-0523, Jan. 2016.

[9]Huff, D. and Henderson, B., "The Aeroacoustics of Offset Three-Stream Jets for Future Commercial Supersonic Aircraft," AIAA 2016-2992, June 2016.

[10]Lighthill, M., "On Sound Generated Aerodynamically: I. General Theory," *Proceedings of the Royal Society of London*, Vol. 211, 1952, pp. 564–587.

[11]Morris, P. J. and Farassat, F., "Acoustic Analogy and Alternative Theories for Jet Noise Prediction," *AIAA Journal*, Vol. 40, No. 4, 2002, pp. 671–680.

[12]Morris, P. and Boluriaan, S., "The Prediction of Jet Noise from CFD Data," AIAA 2004-2977, May 2004.

[13]Goldstein, M. and Leib, S., "The Aeroacoustic of Slowly Diverging Supersonic Jets," *Journal of Fluid Mechanics*, Vol. 600, 2008, pp. 291–337.

[14]Depuru Mohan, N. and Dowling, A., "Jet-Noise-Prediction Model for Chevrons and Microjets," *AIAA Journal*, Vol. 54, No. 12, 2016, pp. 3928–3940.

[15]Leib, S., "Modeling Sound Propagation Through Non-Axisymmetric Jets," NASA/CR–2014-218107, March 2014.

[16]Harper-Bourne, M., "Jet Near-Field Noise of Combat Aircraft," AIAA 1999-1838, May 1999.

[17]Papamoschou, D. and Rostamimonjezi, S., "Modeling of Noise Reduction for Turbulent Jets with Induced Asymmetry," AIAA 2012-2158, June 2012.

[18]McLaughlin, D., Morrison, G., and Troutt, R., "Experiments on the Instability Waves in a Supersonic Jet and their Acoustic Radiation," *Journal of Fluid Mechanics*, Vol. 69, 1975, pp. 73–95.

[19]Tam, C. and Burton, D., "Sound Generation by the Instability Waves of Supersonic Flows. Part 2. Axisymmetric Jets," *Journal of Fluid Mechanics*, Vol. 138, 1984, pp. 273–295.

[20]Mathieu, J. and Scott, J., *An Introduction to Turbulent Flow*, Cambridge University Press, Cambridge, 2000.

[21]Doty, M. and McLaughlin, D., "Space-Time Correlation Measurement of High-Speed Axisymmetric Jets Using Optical Deflectometry," *Experiments in Fluids*, Vol. 28, March 2005, pp. 415–425.

[22]Morris, P. and Zaman, K., "Velocity Measurements in Jets with Application to Jet Noise," *Journal of Sound and Vibration*, Vol. 329, 2010, pp. 394–414.

[23]Viswanathan, K., Underbrink, J., and Brusniak, L., "Space-Time Correlation Measurements in the Near Field of Jets," *AIAA Journal*, Vol. 49, 2011, pp. 1577–1599.

[24]Powers, R., McLaughlin, D., and Morris, P., "Noise Reduction with Fluidic Inserts in Supersonic Jets Exhausting Over a Simulated Aircraft Carrier Deck," AIAA 2015-2374, June 2015.

[25]Mani, R., "The Influence of Jet Flow on Jet Noise. Part 1. The Noise of Unheated Jets," *Journal of Fluid Mechanics*, Vol. 73, No. 4, 1976, pp. 753–778.

[26]Tam, C. and Auriault, L., "Mean Flow Refraction Effects on Sound Radiated from Localized Sources in a Jet," *Journal of Fluid Mechanics*, Vol. 370, 1998, pp. 149–174.

[27]Lighthill, M., "On Sound Generated Aerodynamically. II. Turbulence as a Source of Sound," *Proceedings of the Royal Society of London*, Vol. 222, 1954, pp. 1–32.

[28]Harper-Bourne, M., "Predicting the Jet Near-Field Noise of Combat Aircraft," AIAA 2002-2424, June 2002.

[29]Harper-Bourne, M., "Jet Noise Turbulence Measurements," AIAA 2003-3214, May 2003.

[30]Papoulis, A., *Probability, Random Variables, and Stochastic Processes*, McGraw-Hill, New York, 1965.

[31]Dowling, A. and Hynes, T., "Sound Generation by Turbulence," *European Journal of Mechanics B/Fluids*, Vol. 23, May-Jun. 2004, pp. 491–500.

[32]Raizada, N. and Morris, P., "Prediction of Noise from High Speed Subsonic Jets Using an Acoustic Analogy," AIAA 2006-2596, May 2006.

[33]Wuttke, J., "Fourier Transform of the Stretched Exponential Function: Analytic Error Bounds, Double Exponential Transform, and Open-Source Implementation libkww," *arXiv:0911.4796v3 [math-ph]*, Sept. 2012, pp. 1–11.

[34]Bateman, H., *Tables of Integral Transforms*, McGraw-Hill, New York, 1954.

[35]Ribner, H., "Quadrupole Correlations Governing the Pattern of Jet Noise," *Journal of Fluid Mechanics*, Vol. 38, 1969, pp. 1–24.

[36]Ho, C., "Near Field Pressure Fluctuations in a Circular Jet," NASA CR-179847, Nov. 1985.

[37]Zaman, K., "Flow Field and Near and Far Sound Field of a Subsonic Jet," *Journal of Sound and Vibration*, Vol. 106, No. 1, 1986, pp. 1–16.

[38]Shanno, D. F. and Phua, K. H., "Minimization of Unconstrained Multivariate Functions," *ACM Transactions on Mathematical Software*, Vol. 6, No. 4, 1976, pp. 618–622.

[39]Papamoschou, D., "Fan Flow Deflection in Simulated Turbofan Exhaust," *AIAA Journal*, Vol. 44, No. 12, 2006, pp. 3088–3097.

[40]Papamoschou, D., Xiong, J., and Liu, F., "Aerodynamics of Fan Flow Deflectors for Jet Noise Suppression," *Journal of Propulsion and Power*, Vol. 24, No. 3, 2008, pp. 437–445.

[41]Jameson, A., Schmidt, W., and Turkel, E., "Numerical Solutions of the Euler Equations by Finite Volume Methods Using Runge-Kutta Time Stepping Schemes," AIAA 1981-1259, January 1981.

[42]Menter, F., "Two-Equation Eddy-Viscosity Turbulence Models for Engineering Applications," *AIAA Journal*, Vol. 32, No. 8, 1994, pp. 1598–1605.

[43]Xiong, J., Nielsen, P., Liu, F., and Papamoschou, D., "Computation of High-Speed Coaxial Jets with Fan Flow Deflection," *AIAA Journal*, Vol. 48, No. 10, 2010, pp. 2249–2262.

[44]Rimmell, A., Mansfield, N., and Paddan, G., "Design of Digital Filters for Frequency Weightings (A and C) Required for Risk Assessment of Workers Exposed to Noise," *Industrial Health*, Vol. 53, 2015, pp. 21–27.